# Combination of $\Delta 47$ and U-Pb dating in tectonic calcite veins unravel the last pulses related to the Pyrenean Shortening (Spain)

Guilhem Hoareau, Nemo Crognier, Brice Lacroix, Charles Aubourg, Nick M.W. Roberts, Nathan Niemi, Mathieu Branellec, Nicolas Beaudoin, Isabel Suárez Ruiz

# Combination of Δ47 and U-Pb dating in tectonic calcite veins unravel the last pulses related to the Pyrenean Shortening (Spain)

Guilhem Hoareau[1], Nemo Crognier[1], Brice Lacroix[2], Charles Aubourg[1], Nick M.W. Roberts[3], Nathan Niemi[4], Mathieu Branellec[1], Nicolas Beaudoin[1], Isabel Suárez Ruiz[5]

1 Universite de Pau et des Pays de l'Adour, E2S UPPA, CNRS, TOTAL, LFCR, UMR5150, 64000 Pau, France

2 Department of Geology, 108 Thompson hall, Kansas State University, Manhattan, KS 66506, USA

3 NERC Isotope Geosciences Laboratory, British Geological Survey, Nottingham, UK

4 Department of Environmental and Earth Science, University of Michigan, USA

5 Instituto de Ciencia y Tecnología del Carbono INCAR-CSIC, Oviedo, Spain

Contact: guilhem.hoareau@univ-pau.fr

## Abstract

Clumped isotopes thermometry (Δ47) and U-Pb dating of carbonates have been used to elucidate the temperature-time conditions of 10 tectonic calcite veins in the hanging wall of the South Pyrenean Frontal Thrust (Spain), the youngest thrust unit in the south-central Pyrenees. The Δ47 values indicate precipitation temperatures below ~90°C, in agreement with fluid inclusion analyses. 6 veins have been successfully dated, giving ages between 61 and 14.5 Ma with all but one value below 24 Ma. On the basis of our new results, we propose that several the studied veins record the end of Pyrenean tectonics in the area during the

Burdigalian, possibly up to the Serravalian, younger than estimates based on magnetostratigraphic data from continental syn-tectonic deposits. Calculated $\delta^{18}O$ values of the precipitating fluid are either very positive, suggesting a local source that has interacted with the host rock, or negative, suggesting the downward incursion of meteoric waters. For undated or pre-burial veins, the $\Delta47$ values derived from temperature history reordering model (THRM) show that the measured $\Delta47$ values may have been significantly altered during burial, preventing their use as a reliable thermal or paleohydrological marker. Although applied to a limited number of samples, these results highlight the great potential of the U-Pb/$\Delta47$ approach to decipher the history of vein or cement formation and fluid flow in complex tectonic zones, provided that (i) the thermal evolution is known and (ii) the extent of clumped isotope reordering is systematically modelled.

**Keywords**: Clumped isotopes; carbonate U-Pb geochronology; veins; fractures; Pyrenees

## 1. Introduction

The links between fracture development and fluid flow in foreland fold and thrust belts has been the subject of active research over the last decades (e.g. Roure et al., 2005 and references therein; Lacroix et al., 2014, 2018; Evans and Fischer, 2012; Beaudoin et al., 2014, 2018; Crognier et al., 2018; Cruset et al., 2020). However, in low-temperature systems the precipitation conditions are often obscured by the scarcity of reliable mineral geothermometers and geochronometers, and by the variable impacts of temperature, precipitation rate, and fluid composition, on authigenic mineral composition (e.g. Dromgoole and Walter, 1990; Saulnier et al., 2012; Crognier et al., 2018).

Clumped isotope thermometry ideally recovers the temperature of carbonate formation without making assumptions about the composition of precipitating water and / or oxygen composition of another mineral phase, as required for conventional stable isotope thermometry (Ghosh, 2006). The recent development of calibrations to temperatures higher than 100°C (e.g., Bonifacie et al., 2017; Lloyd et al., 2018) has allowed $\Delta$47 clumped isotope application to the field of fluid migration along tectonic structures, i.e. the Moab fault (e.g., Bergman et al., 2013; Hodson et al., 2016), the San Andreas Fault Zone (Luetkemeyer et al., 2016), or the Cotiella and Lower Pedraforca thrust faults in the Pyrenees (Lacroix et al., 2018; Cruset el al., 2020). It is also very recently that U-Pb dating of calcite cements by LA-ICPMS has been employed to successfully date brittle faulting and diagenetic cements (e.g., Roberts and Walker 2016; Beaudoin et al., 2018; Mangenot et al., 2018; MacDonald et al., 2019; Cruset et al., 2020). When combined together these techniques may considerably refine the diagenetic and fluid-flow history of sedimentary basins, and increase our understanding of past diagenetic alteration, especially along fault systems (Lawson et al., 2017; Mangenot et al., 2018; MacDonald et al., 2019; Cruset et al., 2020).

Here, we focus on the South Pyrenean Frontal Thrust (SPFT), outlined by the Sierras Exteriores (Spain), a complex alignment of folds and thrusts making the most external part of the South-Pyrenean fold and thrust belt. Although its tectonic and sedimentary evolution has been extensively documented (e.g. Turner, 1988, Millán Garrido et al., 1994; Arenas et al., 2001; Oliva□Urcia and Pueyo, 2007; Oliva-Urcia et al., 2016, 2019), only a few studies have focused on the thermal or paleohydrological history of the SPFT (Beaudoin et al., 2015; Labaume et al., 2016). This example is particularly suitable to test whether the combination of $\Delta$47 clumped isotopes and U-Pb dating of carbonates ($\Delta$47/U-Pb thermochronometry) can bring valuable information about the thermal and fluid-flow evolution in complex fault systems.

In this contribution, $\Delta$47/U-Pb thermochronometry of calcite veins from the SPFT are combined with fracture analysis, fluid-inclusion microthermometry and thermal modeling to define the temperature and timing of vein formation, and to unravel the origin of calcite-precipitating fluid within the tectonic frame of the area.

## 2. Geological Context

The South Pyrenean Frontal Thrust is located at the southern front of the Pyrenees, a double-verging asymmetric fold and thrust belt which developed from the Late Cretaceous to the Early Miocene during the convergence between the Iberian and European plates (Choukroune et al., 1990; Muñoz, 1992; Beaumont et al., 2000; Teixell et al., 2018) (Figure 1A). Most of the central and southern part of the Pyrenees is affected by a series of south-verging thrusts and folds (e.g., Labaume et al., 2016 and references therein; Munoz et al., 2002, 2013, 2018). The Axial Zone is made of imbricated thrust units of Paleozoic basement, which connect southward to thrust units affecting Mesozoic to Cenozoic sediments, forming the South Pyrenean Zone (SPZ), which overrides the Ebro foreland basin (Teixell, 1996; Labaume et al., 2016; Teixell et al., 2018). In the west-central Pyrenees, the SPZ corresponds to the Jaca-Pamplona piggyback basin. From north to south, basement thrusts affecting the SPZ along the eastern Jaca basin transverse include the Eaux-Chaudes-Lakora thrust (Ypresian-Bartonian), the Gavarnie thrust (Priabonian-Rupelian), the Broto thrust (Rupelian-Chattian), and the Fiscal and  Guarga thrusts (late Rupelian-Aquitanian) (Labaume et al., 2016; Oliva-Urcia et al., 2019 and references therein) (Figure1B). The emergence of the SPFT, forming the Sierras Exteriores in the study zone, was contemporaneous to the Broto and Fiscal-Guarga basement thrusts (~33 – 20 Ma), and accumulated at least 22 km of shortening (Labaume et al., 2016). It subdivided the SPZ in the Jaca–Pamplona basin and the Ebro basin.

The Sierras Exteriores consist of a complex WNW-ESE alignment of thrusts, which cross several anticline folds (from the east to the west: Gabardiella, Pico del Aguila, Bentué de Rasal, Santo-Domingo anticlines) (Anastasio, 1987; Millán Garrido et al., 1994, 2000; Arenas et al., 2001) (Figure 1C, D, E). The Gabardiella, Pico del Aguila, Bentué de Rasal and Rasal anticlines formed  along with Eaux-Chaudes and Gavarnie thrust activities, and have been interpreted to have formed on oblique ramps of south-verging thrusts (e.g., Pueyo et al., 2002), or as a result of westward propagation of deformation during early Bartonian to Priabonian times (Labaume et al., 2016; Mochales et al., 2012). They have a rough N-S axial orientation, explained by a syn-growth clockwise rotation of up to 40° (Pueyo et al., 2002; Huyghe et al., 2009). The WNW-ESE Santo Domingo anticline formed during Rupelian to Aquitanian times, coeval to the Broto and Fiscal thrusts (Oliva-Urcia et al., 2019).  The folds were affected by the emergence of cover thrusts collectively labeled as the Sierras Exteriores thrust by Labaume et al. (2016). These thrusts correspond to the cover equivalent of the Fiscal-Guarga thrusts, and form the SPFT. Although their activity is clearly recognized between the Rupelian and the Aquitanian (e.g., Oliva-Urcia et al., 2019), minor, active compressive tectonics has been proposed to have taken place at least until the Burdigalian, as the uppermost Aquitanian continental deposits of the Uncastillo Formation are folded and thrusted (e.g., the Domingo-Gabardiella thrust sytem; Millán Garrido et al., 2000; Arenas et al., 2001). In the Pico del Aguila fold, this complex evolution was associated with the development of a polyphase fracture network from the Paleocene to the Oligocene, associated with a multi-stage fluid flow history involving both local waters and the ingress of meteoric water from the surface (Beaudoin et al., 2015).

From the early Eocene to the Miocene, the activity of the successive southward-verging thrusts was contemporaneous with deposition of several thousand meters of syntectonic sediments in the Jaca-Pamplona basin, above Triassic to Paleocene pre-tectonic sediments (e.g., Soler-Sampere and Puigdefàbregas, 1970; Carbayo et al., 1972; De Rojas and Latorre, 1972; Samso et al., 1991; Teixell et al., 1992; Montes and Barnolas, 1992, 2002;

Millán Garrido et al., 1994, 2000; Arenas et al., 2001; Oliva-Urcia et al., 2016, 2019; see also references used for thermal modelling in the Supplementary Material) (Figure1B). Based on the references cited above, in the Sierras Exteriores, pre-tectonic sediments include middle Triassic carbonates, upper Triassic shales and evaporites (10-100 m), upper Cretaceous limestones (Adraen-Bona Formation, 50-250 m), and Cretaceous / Paleocene continental deposits (Garumnian Formation, 10-100 m). Overlying syn-folding deposits are marked by significant variations in thickness. They include marine Lutetian platform limestones (Guara Formation; 50-800 m), grading upward into the marine marls of the Arguis-Pamplona Formation (Bartonian; 300-1000 m), and deltaic sandstones (Belsué-Atarès and Yeste-Arrés Formations, Bartonian-Priabonian, 10-200 m). Emersion of the entire Jaca-Pamplona basin during the Priabonian-Chattian was marked by the westward progradation of the Campodarbe conglomerates (~1000-3500 m), uncomfortably overlain by the Uncastillo conglomerates (late Chattian-Aquitanian, ~200-500 m).

The thermal evolution of the SPFT remains poorly constrained. According to Labaume et al. (2016), the Triassic deposits presently outcropping in the Sierras Exteriores were buried up to ~5 km. Assuming a geothermal gradient of 24 °C/km typical of foreland basins (Allen and Allen, 2013), this would correspond to maximum temperatures of ~140 °C in the studied zone. Such temperature is grossly consistent (i) with the temperatures of ~80-100 °C proposed by Cantarelli (2011) in the Belsué-Atarés and Arguis-Pamplona Formations north of the Rasal anticline (~4 km burial), (ii) with the absence of resetting of apatite fission track ages in Belsué-Atarés sandstones sampled east of the Arguis anticline (Labaume et al., 2016), and (iii) with the low precipitation temperatures of veins sampled in the Pico del Aguila anticline by Beaudoin et al. (2015) ($T < 100$°C).

## 3. Methodology

3.1. Sampling and analytical strategy

The initial sampling strategy was intended to increase knowledge of the thermal evolution of the Sierras Exteriores. 17 outcrops of Triassic to Rupelian sedimentary rocks were selected to sample bulk rocks and/or calcite veins (Figure 1B, C, D). 9 bulk rocks appeared suitable for the measurement of vitrinite reflectance (VR) or Rock-Eval (RE) Tmax values, and were used to build 1D thermal models of the study area. 10 tectonic calcite veins scattered along the Sierras Exteriores were selected to assess fluid temperature conditions both from fluid inclusion data and from Δ47 clumped isotope analysis (SE1, SE2, SE3, SE4, SE10, SE12, SE13, A21, A22, and A56). Among the veins, three were previously sampled in the Pico del Aguila anticline (A21, A22, and A56, corresponding to sites 436, 439 and 467, respectively, in Beaudoin et al. (2015)). Vein sampling was associated with the analysis of fracture and vein orientations where outcrop conditions permitted (7 veins out of 10: sites SE4, SE10, SE12, SE13, A21, A22, A56), in order to link vein formation to the main tectonic events recorded in the Sierras Exteriores. Given the maximal burial temperatures obtained from VR, RE Tmax values and thermal modelling (T > 100°C; see Results section), U-Pb dating of these calcite veins was then performed to estimate the degree of Δ47 solid-state reordering which, depending on the thermal history, can lead to erroneous Δ47 temperatures (TΔ47) (Lloyd et al., 2018).

3.2. Analytical methods

Petrographic and microstructural characteristics of the veins were studied on polished thick- and thin-sections using optical microscopy and cathodoluminescence (CL). CL images were acquired using an OPEA Cathodyne coupled to a Nikon BH2 microscope at the University of Pau and Pays de l'Adour (LFCR, France). Analytical conditions were with an accelerating voltage of 12.5 kV and an intensity of 200–300 mA.

Fluid-inclusion petrography was performed on doubly polished thick sections (100 µm) of the vein samples using a Linkam automatic THMSG600 cooling–heating stage coupled to a Nikon LV-150-ND microscope and a Nikon MK1 camera (University of Pau, LFCR, France). Calibration of the microthermometric stages used synthetic fluid inclusions (FIL, Leoben, Austria), including, (1) pure water (ice melting temperature (Tm) = 0.0 °C; critical homogenization temperature (Th) = 374.1 °C), (2) $H_2O$-$CO_2$ inclusions ($CO_2$ melting temperature = -56.6 °C; hydrate melting temperature = +9.9 °C) and (3) $H_2O$-NaCl inclusions (eutectic temperature (Te) = -21.2 °C). Accuracy was ±0.1 °C at temperature between -56.6 and +25 °C and ±2 °C at +374 °C. Progressively heating up to Th was followed by freezing of the inclusions, and their slow heating to tentatively determine their Te and Tm.

Carbon and oxygen isotopes as well as Δ47 clumped isotopes compositions of the 10 vein calcite samples were performed at the University of Michigan. About 6 mg of micro-drilled carbonate powder was loaded into a manual multi-sample rotary carrousel. Each sample was then dropped into ~20 ml of anhydrous 105 wt. % phosphoric acid maintained at 75°C. Extracted $CO_2$ was purified following cryogenic procedures (propanol and liquid N2 mixture at -95°C) under vacuum conditions as defined in Ghosh et al. (2006) and Huntington et al. (2009), to remove residual water vapor. $CO_2$ was then purified to remove any hydrocarbon and halocarbon contaminants by passing through Porapak™ resin at ~ -35°C for 15 min. Finally, purified $CO_2$ was transferred to a vial for storage for no more than 24 hr before analysis. $CO_2$ masses 45-49 were measured on a dual-inlet Thermo-Finnigan MAT 253 mass spectrometer following the methods of Huntington et al. (2009). Δ47 values were calculated using the stochastic reference heated gas and equilibrated $CO_2$-water (at 25°C) lines produced during the relevant analysis period (March 2014, September 2014 and January 2015). Heated gas was produced by heating $CO_2$ gases of different isotopic compositions in a furnace for 2 hr. Each isotopologue analysis required ~2 ½ hr of mass spectrometer time to achieve precisions on the order of 10-6 for Δ47 values and each carbonate sample was analyzed at least 3 times in order to reduce uncertainties in derived Δ47 temperature values. Final temperature values were corrected empirically for acid fractionation factor at 75°C (Guo et al., 2009). Δ47 results are normalized to the Universal Reference Frame as proposed by Dennis et al. (2011) using $CO_2$-$H_2O$ equilibration at 25°C and heated $CO_2$ at 1000°C. Δ47 values are converted into temperatures using the Δ47-temperature calibration of Bonifacie et al. (2017).

For the host rock samples, O- and C-isotopes analysis was performed at the ISTeP (Paris, France), using a Kiel IV Carbonate device connected to a mass spectrometer delta V advantage. About 40 µg of calcite powder was reacted with 104% phosphoric acid at 70 °C in individual vials. The $CO_2$ sample gas produced was purified in an automatic cryogenic system. Instrument calibration was performed using the standard NBS 19 and an in-house standard (Marceau). The analytical precision determined by analysis of NBS 19 was 0.07‰ for $\delta^{18}O$ and 0.03‰ for $\delta^{13}C$. Carbon and oxygen isotopic composition are reported as relative to Vienna Pee Dee Belemnite (VPDB).

U-Pb geochronology via the in-situ LA-ICP-MS method was conducted at the Geochronology & Tracers Facility, NERC Isotope Geosciences Laboratory (Nottingham, UK). The method utilizes a New Wave Research 193UC excimer laser ablation system, coupled to a Nu Instruments Attom single-collector sector-field ICP-MS. The laser parameters used are a 100 µm static spot, fired at 10Hz, with a ~7-8 j.cm$^2$ fluence, for 30 seconds of ablation. Normalization uses standard sample bracketing to NIST 614 glass for Pb-Pb ratios, and the WC-1 carbonate reference material for $^{206}Pb/^{238}U$ ratios (Roberts et al., 2017). Normalisation is based on the measured/accepted ratio derived from the session-based drift-corrected mean of the primary WC-1 reference material. An additional carbonate material, Duff Brown, was measured in most sessions to provide a control on accuracy and precision. No common lead correction is made; those ages that are deemed robust (based on low MSWD), are determined from lower intercepts on a Tera-Wasserburg plot. Age results are based in lower intercept ages with systematic uncertainties (decay constants, reference material age uncertainty, long-term method reproducibility) propagated. Resulting ages have uncertainties quoted as age ± x/y, where x is without systematic uncertainties and y is with (see Horstwood et al., 2016). Additional information is available in the Supplementary Material.

Vitrinite reflectance analyses were performed at the INCAR laboratory (Oviedo, Spain), using reflected white light and an oil immersion objective (50x) in an MPV-Combi-Leitz optical microscope. The petrographic pellets were prepared using a procedure described in the ISO norm (ISO-7404-2, 2009). These pellets are formed by 10-15 g of rock, grounded until a particle size of about 1 mm, blended with a synthetic resin composed by styrene and phthalic anhydride. Rock particles stiffened in the resin in a random statistical orientation. The resulting samples were polished and put for minimum 24 hours in a silica-gel drier before microscopic analysis. All samples were examined under reflected white light. The reflectance was measured in incident white light on vitrinite particles of unaltered / unoxidized samples, following the ISO-7404-5 (2009) and ASTM-D7708-11 (2011) norms.

Rock-Eval pyrolysis was made using a Rock Eval 6 (VINCI Technologies), at the ISTeP (Paris, France), in order to obtain RE Tmax values, which corresponds to the temperature at which the largest quantity of hydrocarbons is released upon cracking.

## 4. Results

### 4.1. Analysis of fracture and vein orientation

The statistical analysis of the fracture network was focused on measurements of joints and veins that exhibit no evidence of shear, at sites SE4, SE10, SE12, and SE13. These data were complemented with previously published data from 3 sites (A21, A22, A56) (Beaudoin et al., 2015). The three stereograms proposed for each site (Figure 2) correspond to the present-day orientations, and to orientations corrected for deformation recorded in the Sierras Exteriores (folding of strata, and regional tilting due to activation of the Guarga thrust, taken as a plane N110°E/30°NE (strike/dip) following Beaudoin et al., 2015). Examples of field photographs of joints and veins are presented in Figure 3A to 3D.

For this study, the veins were sampled in stratigraphic levels ranging from the Triassic to the Priabonian. In the Bartonian / Priabonian Arguis-Pampelune marls (sites A21 and A22), most veins are oriented N060°E, and become vertical after unfolding and backtilting. To a lesser extent, N170°E striking fractures are also found. Note that vein A22 was interpreted as a right-lateral fault by Beaudoin et al. (2015). In the Lutetian Guara limestones (sites SE4 and A56), the fracture patterns are similar at both sites, with N110°E preferential orientation, along with a minor N170°E trending set. The latter is orthogonal to bedding in current bedding attitude, whereas the other one is not. In the Cretaceous Adraen Bona formation (site SE12), most fractures are vertical after unfolding and backtilting, trending along the N170°E and N110°E directions. In the middle Triassic (Muschelkalk) beds (sites SE10 and SE13), the fractures are vertical after the same corrections, and 4 trends of fractures striking N060°E, N140°E, N170°E and N040°E are recognized. The N060°E-striking fractures are restricted to the Triassic and Bartonian / Priabonian beds, whereas the N110°E-striking fractures are found both in the Muschelkalk and Eocene limestones. Finally, the N170°E-striking fractures has been measured in all lithologies, and the N140°E-striking fractures are only seen at SE10.

4.2. Vein petrography

Nine of the 10 collected veins consist to either mode I extensional veins or mode I-mode II transtensional shear veins according to the nomenclature of Bons et al. (2012). Only one vein (SE2) corresponds to the mode II (shear vein). Extensional veins (SE1, SE3, SE4, SE10, SE12, SE13, A21 and A56) correspond to mm- to cm-thick veins, filled by granular, blocky or elongated-blocky calcite. Among them, 2 veins (SE1, A56) show evidence of crack-seals events, indicating precipitation coeval to fracture opening. The former one displays multiple crack-seals on the borders and elongated blocky calcite crystals, defining a stretching vein (Bons et al., 2012) (Figure 3E). The latter one is filled by blocky crystals, mixed with pieces and trails of host-rock (Figure 3F). One vein (SE4) is characterized by blocky crystals affected by several stylolites parallel to the vein walls (Figure 4A). The other extensional veins are filled with blocky calcite without evidence of syn-opening precipitation (Figure 4E).

The transtensional shear vein (A22) has a thickness of 2.5 cm. It presents a first generation of elongated blocky crystals slightly oblique to the vein walls, corresponding to a first stage of opening (Figure 4B). It is followed by elongated blocky crystals evolving to large blocky crystals towards the center of the vein, corresponding to a second stage of opening and calcite precipitation.

The shear vein (SE2) corresponds to a cm-thick body featuring slickenfibres. Microscopically, it comprises stacked (sub)-millimeter thick sheets parallel to the macroscopic vein, formed by the lateral succession of numerous sub-millimetric rhomb-shaped veinlets separated from each other by thin, locally discontinuous, host-rock bands (Figure 4C), similar to the description of Bons et al. (2012; their Fig. 12).

Five veins (A56, SE2, SE4, SE12, SE13) present a homogeneous CL, supporting a single precipitation stage or precipitation from waters with similar composition (Machel, 2000). They have a dull orange-red color in CL, except SE13 where the CL is extinct. The five other veins present at least two distinct colors. Among these, three veins (A21, SE3, SE10) show concentric CL zoning in the blocky calcite grains, reflecting precipitation under variable redox conditions or variations in precipitation kinetics (Machel, 2000). In A21 and

SE3 veins, the CL zonings remain in orange tones (Figure 4E). In SE10 vein, they evolve from orange, to dull and bright yellow, supporting multi-precipitation stages (Figure 4D). Finally, in A22 vein, the CL varies slightly between the 2 cement precipitation stages (dull orange on the borders to brighter orange to the center of the vein) (Figure 4B), whereas for SE1 the fringe of crystals having partially filled some voids have an orange CL brighter than in the rest of vein (Figure 3E).

4.2. Fluid inclusion petrography and microthermometry

All veins show small primary and secondary fluid inclusions (generally below 5 µm), making phase transition temperatures difficult to measure. Only 3 samples (SE2, SE10 and SE12) presented primary two-phase aqueous inclusions with Th in the range 75˚C-83°C for sample SE2 (n = 5), 125-185°C for sample SE10 (n = 4) and 79-95°C for sample SE12 (n = 6) (Figure 5A; Table S1). For SE10, most primary fluid inclusions were all liquid, suggesting that the few two-phase inclusions are the results of variable inclusion stretching. The other veins show only single-phase primary inclusions, generally suggesting trapping temperatures below 50°C, or up to ~100°C for very small inclusions (< 3 µm) (Goldstein and Reynolds, 1994). The same conclusion applies to the secondary inclusions, which are all liquid in all the veins. No Te and Tm could be measured.

4.3. Stable and Δ47 clumped isotopes

For the analyzed veins, the $\delta^{18}O$ and $\delta^{13}C$ values range between -9.24‰ and +2.69 ‰ VPDB, and between -4.47‰ and +1.22‰ VPDB, respectively (Figure 5C; Table S1). Their Δ47 values range from 0.696‰ to 0.532‰, which can be converted to precipitation temperatures between 21˚C and 88 ˚C (Figure 5B; Table S1). For the three veins presenting two-phase aqueous fluid inclusions, the TΔ47 values are in good agreement with the homogenization temperatures (Figure 5B).

For the host rocks, the isotopic composition range between -2.37‰ and +2.71‰ VPDB for $\delta^{13}C$, and between -6.52‰ and -2.73 ‰ VPDB for $\delta^{18}O$ (Figure 5C).

4.4. Carbonate U-Pb dating

Two to 6 transects of spot ablations were performed in 8 of the 10 vein samples selected for U-Pb dating. 6 samples (SE3, SE4, SE10, A21, A22, A56) gave meaningful, accurate ages (that we define as being younger than the depositional age of the enclosing rocks and older than present within 2 sigma uncertainties, and as having MSWD below 2), for at least one transect. Note that sample A21 is included in the successful samples, despite a MSWD of 2.5. The ages obtained range from 60.7±2.9 Ma to 14.4±2.7 Ma (Figure 6; Table S1 and S2). They correspond to one transect (A56, SE10), or from the combination of two transects giving ages similar within uncertainty (A21, A22, SE3, SE4). All veins but one show precipitation ages younger than ~24 Ma (23.8 Ma to 11.7 Ma if the age uncertainties are considered).

4.5. Maturity of organic matter

Accurate vitrinite reflectance values could be measured on only 3 samples (1 coal sample in the Triassic (site SE11) and 2 limestone samples in the Cretaceous (site SE12)) (Figure 1). The values are 0.32±0.04% (1s) for sample SE11, and 0.34±0.03% and 0.44±0.10% for sample SE12 (n = 12) (Figure S2). For Rock-Eval analyses, measurements were performed on 17 powdered samples mostly from the northern part of the study zone. Only 7 samples yielded reliable RE Tmax values varying from 431 to 443°C (Figure 1B, Table S3).

## 5. Discussion

5.1. Timing of joint and vein emplacement in the SPFT: structural measurements versus U-Pb dating

Our novel data of fracture orientation (i.e., joints and veins), combined with existing interpretation of the Pico del Aguila anticline (sites A21, A22 and A56; Beaudoin et al., 2015) allow to propose a sequence of deformation in the Sierras Exteriores. Based on fracture orientations and their link with local fold axis orientation, we first discuss whether the main fractures sets, which comprise the vein analyzed, formed before, during or after folding (see Tavani et al., 2015). We propose that at 4 sites, there are 2 main fracture sets developed before folding, or during early folding: one set trending ~N060°E comprising fractures at high-angle to bedding (A21, A56, SE10, SE13), and one set trending ~N170°E (SE10, SE12, SE13). At 2 sites (A22 and SE4), the dominant fracture sets are identified as being late- to post- folding in origin. For site A22, Beaudoin et al. (2015) have shown that the veins result from the reactivation of former joint during Guarga thrusting. For site SE4 (located at the eastern tip of the Santo Domingo anticline), our interpretation is based both on the present-day vertical orientation of the main set, and on its mean strike similar to the fold axis (~N110).

Where U-Pb dating was successful (A21, A22, A56, SE4, SE10), we can refine this interpretation with absolute age constraints. For sites A21 and A56, formation of the ~N060°E directed fractures (which include the veins dated) during early folding of the Pico del Aguila anticline, as proposed by Beaudoin et al. (2015), would correspond to the Bartonian (~38-41 Ma). U-Pb ages show that these fractures actually are cemented with calcite dated to ~14-16 Ma. For sample A21 (14.7 ± 2.7 Ma), whether the cement is contemporaneous or younger than the opening of the fracture cannot be answered from petrographic observations. However, for sample A56, the young age (16.6 ± 1.1 Ma), added to evidence of syn-tectonic calcite precipitation, suggest that the fracture developed only after the activation of the Guarga thrust (i.e., post-folding), or that the crack-seal may have reactivated an inherited fracture. For site SE10 (Triassic Muschelkalk beds located south-west of the Pico del Aguila anticline), relation to folding of the early ~N060°E-striking set would lead to interpret it as related to Layer Parallel Shortening (LPS; sensu Bergbauer and Pollard, 2004). U-Pb dating (60.7 ± 2.9 Ma) demonstrates that instead, these fractures developed prior to LPS, before regional clockwise rotation, leading us to interpret them as the across-strike set of fractures of the foreland forebulge (sensu Tavani et al., 2015). Accordingly, the other fractures of this site (~N170°E-striking) correspond to the along-strike set. For sample A22, the interpretation of a post-folding vein development is compatible with the measured U-Pb age (18.8 ± 5.0 Ma). Finally, for site SE4, the main fracture set likely formed at the end of Santo Domingo folding. According to Oliva-Urcia et al (2019), this fold developed during Chattian-Aquitanian times (~20-27 Ma), slightly older than our U-Pb age of 17.3 ± 3.4 Ma. Petrographic evidence of vertical stylolites in the vein demonstrates clearly that tectonic shortening was still ongoing after vein precipitation, i.e. at least during the Burdigalian.

The consequences of the interpretations proposed above are twofold. First, although based only on a limited set of data, the ages obtained by U-Pb dating of calcite veins have bring decisive insights into the sequence of deformation recorded in the SPFT. For some veins (A56 and SE10), absolute age determinations were in contradiction with the interpretations based solely on the study of fracture sets (i.e., younger and older, respectively). We propose that the structural approach to determining relative joint/vein ages in folds should be systematically associated with absolute dating of vein precipitation for greater reliability, as proposed by Beaudoin et al (2018) in the Bighorn Basin (USA). Second, U-Pb dating alone suggests that the SPFT may still have recorded tectonic shortening after 17.3 ± 3.4 Ma at least in the Santo Domingo area, as shown by the results obtained on sample SE4. This age is slightly younger than the minimum age of ~20 Ma proposed by Oliva-Urcia et al. (2019) in their paleomagnetic and tectono-sedimentary study of the Uncastillo Formation at the southern flank of the Santo Domingo anticline. However, it is in accordance with observations that in the same anticline, the uppermost conglomerates of the Uncastillo Formation were folded and thrusted by the Domingo-Gabardiella thrust system, suggesting deformation during the Burdigalian (Millán Garrido et al., 2000; Arenas et al., 2001). The other veins that formed after the Aquitanian (A21, A56, SE3) have ages similar to that of sample SE4 within uncertainties, and may also have formed in response to compressive deformation in the SPFT. However, in the absence of petrographic evidence of such deformation, alternative scenarios of joint/vein development may also be considered. For A21 and SE3 veins, which do not present evidence of syn-opening precipitation, they include the possibility of a time gap between fracture opening and calcite precipitation, as locally observed in the Bighorn Basin (Beaudoin et al., 2018). For all three samples, joints may have formed earlier (during the Bartonian for A21 and A56) before being reactivated as veins. Finally, for SE3 vein, in the absence of statistical analysis of the fracture network, the development of joint/vein during post-tectonic exhumation cannot be excluded (Engelder, 1985; Twiss and Moores, 2006). Nevertheless, our results suggest that fractures can record subtle deformations that would have remained unrevealed with other methods such as the study of tectono-sedimentary relationships. Absolute U-Pb dating of veins provides a robust time frame to these movements, allowing to refine previous interpretations of the tectonic evolution of geologically complex areas such as the SPFT.

## 5.2. Thermal evolution of the SPFT and impact on TΔ47 values

### *5.2.1. 1D Thermal modelling of the SPFT*

Little quantitative data is available on the thermal evolution of the Sierras Exteriores area. To our knowledge only Cantarelli (2011) has proposed maximum burial temperatures of ~80-100°C in the Belsué-Atarés and Arguis-Pamplona Formations, based on vitrinite reflectance and illite crystallinity. To better constrain this thermal evolution, we used our vitrinite reflectance (VR) and RE Tmax values to perform 1D thermal models along 4 virtual stratigraphic wells (San-Felices, Riglos, Nueno and Pico del Aguila from west to east) constructed from compilations of thickness and age of deposition data available in the literature (Figure 7; see the Supplementary Material for details of the approach). The VR measured at the base of each virtual stratigraphic well (0.3 to 0.4%) are abnormally low given thickness of the stratigraphic pile (> 1.5 km before uplift-related erosion), and the VR measured in the Campodarbe Formation (0.3±0.1%) by Izquierdo-Llavall et al (2013). The delay or suppression of vitrinite reflectance has been recognized in various geological contexts and lithologies, and is commonly explained by a hydrogen-rich vitrinite composition or by the development of overpressures (Price and Barker, 1985; Carr, 2000). For this reason, only the thermal models built with the values of RE Tmax have been retained. The RE Tmax values measured in the upper part of the sedimentary columns (431 to 443°C) are all consistent with the onset of the oil window, equivalent to VR of at least ~0.5-0.6% (Lafargue et al., 1998). Using these values in the models results in temperatures of 120 to 140°C at the base of the virtual stratigraphic wells at ~28 Ma, corresponding to the onset of the Fiscal-Guarga thrust (Labaume et al., 2016), and taken as the time of maximum burial before exhumation of the Sierras Exteriores. Such values are equivalent to a VR of ~1.1 to 1.3% (Figure 7). They require adding to the composite logs a substantial thickness of sediments (1 to 2 km) that would currently be eroded, leading to an initial thickness of ~2.5 to 3.5 km for the Campodarbe Formation. These values are compatible with those measured on either side of the Sierras Exteriores (Millán Garrido et al., 1995), as are the burial temperature estimates based on RE Tmax values compatible with Cantarelli (2011) estimates and Labaume et al. (2016) reconstructions. Exhumation rates in the southern Pyrenees from the Upper Oligocene are little constrained, notably due to debates about the thickness, spatial extent and timing of the erosion of late- and post-orogenic continental deposits (e.g., Coney et al., 1996; Babault et al., 2005). Therefore, we chose to apply two different, simple exhumation scenarios to the wells. The first scenario implies a temperature of 40°C (1.5 km of burial) at 20 Ma and a current temperature of 15°C at the surface (based on Labaume et al., 2016). In the second scenario, we consider a linear temperature decrease between ~28 Ma and present times. Using these constraints, thermal modelling suggests that all dated veins except SE10 are likely to have precipitated in thermal equilibrium with their host rock (Figure 8).

*5.2.2. Modelling the effects of solid-state reordering on TΔ47*

It is well known that carbonates can undergo solid-state reordering during diagenesis, resulting in the alteration of their initial Δ47 values (e.g. Passey and Henkes 2012; Stolper and Eiler 2015; Lawson et al., 2017; Lloyd et al., 2018). Based on an experimental approach, Lloyd et al. (2018) demonstrate that the kinetic of reordering of carbonate can be constrained by the reaction-diffusion model proposed by Stolper and Eiler (2015). This model incorporates both diffusion of isotopes through the crystal lattice and isotope-exchange reactions between adjacent carbonate groups (see Stolper and Eiler 2015 for a complete description). Here, we use a temperature history reordering model (THRM) to explore the kinetic re-ordering of Δ47 of the studied calcite veins, by integrating the reaction-diffusion model of Stolper and Eiler (2015) (using the numerical code from Lloyd et al., 2018) with the thermal history derived from our 1D thermal modelling, and when available, the measured U-Pb ages.

It is worth noting that among the 6 veins dated, the 5 ones having ages younger than 23.8 Ma were formed during exhumation, about 9 to 13 Ma after maximum burial (taken as ~28 Ma). According to the 1D thermal model, they did not encompass temperatures higher than 80°C. Experimental and theoretical considerations have shown that clumped isotope reordering is very limited at such low temperatures (< 100°C; e.g., Passey and Henkes 2012; Stolper and Eiler, 2015; Lloyd et al., 2018). For these veins, the TΔ47 values, which lie below ~80°C, reflect the true precipitation temperature (Table S1). In contrast, the THRM suggests that the vein sample SE10, dated at ~61 Ma, has undergone significant reordering resulting in a measured TΔ47 higher than the temperature at the time of precipitation, due to burial temperatures higher than 100°C at ~28 Ma. Assuming precipitation temperature identical to the enclosing rocks temperature of ~40°C (as deduced from 1D thermal modelling at 61 Ma), the TΔ47 values calculated by the THRM can vary between ~45 and ~80°C, if considering the 2σ uncertainties at the output of the model (Figure 9A). This temperature range is similar to measured TΔ47 values (Table S1). Considering different temperature conditions of SE10 vein precipitation (for example, 20 and 80°C) results in different reordering pathways, but the final modelled TΔ47 temperatures can yet be similar to the measured TΔ47 values. The same conclusion can be drawn for the 4 veins that could not be dated (SE1, SE2, SE12 and SE13). Taking SE2 as an example, temperatures calculated with the THRM fall in the same measured TΔ47 range (77-97°C) if the veins formed between ~75°C and ~110°C during burial (Figure 9B), or if they formed between ~80°C and ~110°C during exhumation (Figure 9C). The measured TΔ47 can then be equally explained by precipitation at different temperatures and ages (between ~32 Ma and ~24 Ma). Therefore, reordering modelling shows that modelled present-day Δ47 temperatures can result from various reordering pathways depending on the age of precipitation (i.e. no significant reordering for late precipitation, or consequent reordering for early precipitation), even for a thermal peak limited in both duration and intensity (< 10 Ma at 100-140°C). In general, the example of the SPFT demonstrates that the use of clumped isotope reordering models based on thermal history should be systematically applied in clumped isotope studies of sedimentary basins, if there is evidence of burial temperature exceeding ~100°C, especially when the ages of carbonates are not precisely constrained.

5.3. Paleohydrology of the SPFT during late tectonics

In order to gather information on the paleohydrology recorded in the Sierras Exteriores during the last tectonic pulses, we derive the $\delta^{18}O$ values of the waters at the origin of the precipitation of calcite veins ($\delta^{18}Ow$). To do this, we use both the TΔ47 and $\delta^{18}O$ values of calcite veins and the oxygen isotope fractionation factor of Kim and O'Neil (1997). For the reasons mentioned in the previous section, we focus on the 5 samples for which we obtained precise and recent U-Pb ages. For these veins, the $\delta^{18}Ow$ shows large variations with values ranging from -4.5‰ to +10.3‰ VSMOW (Figure 5D). All the veins considered in this study are hosted within marine sediments. $\delta^{18}Ow$ values of unaltered marine water source should be ~ -1‰ VSMOW (Zachos et al., 2001). Such values are not recorded in our studied veins suggesting either that (i) the water has been isotopically altered by interaction with the host sediments, or (ii) the veins record water incursions from external reservoirs. The most negative values observed in the SE3 and A56 veins (mean values of -2.6 and -4.5‰, respectively) are compatible with a meteoric source (Longstaffe, 1987), which require infiltration of external water. Considering the young precipitation age of these veins (~16-18 Ma), and therefore their formation after the uplift of the area during the Priabonian (Labaume et al., 2016), the incursion of meteoric waters from the surface is not surprising (e.g., Beaudoin et al., 2015; Roure et al., 2005; Lacroix et al., 2014). The very low TΔ47 obtained for SE3 vein, which requires the incursion of water colder than the enclosing rock, further reinforces this interpretation. The 3 other veins which formed after 25 Ma (SE4, A21, A22) have $\delta^{18}Ow$ values between +4.7 and +10.3‰. These high values are consistent with water isotopically buffered by host rocks during burial history, or with the involvement of highly evaporated water (Bradbury and Woodwell, 1987; Longstaffe, 1987). If fluid flow has occurred, it has not acted long enough or in a volume sufficient to maintain an oxygen isotopic imbalance of oxygen with the host rocks (e.g., Bradbury and Woodwell, 1987).

The $\delta^{13}C$ values of the youngest veins are generally homogeneous, ranging from -0.9 to +0.9‰, values compatible with waters of marine origin or having been isotopically buffered by marine carbonate rocks. Only the SE3 vein shows a significant difference with its host rock (+0.1 versus -1.6‰), which is once again in the direction of an incursion of water in isotopic imbalance with the surrounding rock. To summarize, the late veins studied show two distinct paleohydrological regimes, with either evidence of meteoric water circulation or the presence of isotopically buffered waters and therefore possibly of more local origin. The recording of these two sources of fluids in tectonic veins is consistent with other continental fold and thrust belts (e.g., Roure et al., 2005 and references therein; Travé et al., 2007; Cruset et al, 2020). Examples include the Canadian Rockies (Garven, 1985), the Mexican fold and thrust belt (Fitz-Diaz et al., 2011), the Albanides (Vilasi et al., 2009), but also the central and eastern South Pyrenean fold and thrust belt, as shown in the Jaca and Cotiella thrusts (Lacroix et al., 2014; Travé et al., 1997) or the Lower Pedraforca thrust sheet (Cruset et al., 2020). In all these settings, and as we infer in the SPFT, marine-derived or isotopically buffered waters were dominant in volume, but topographic highs acted as recharge areas for meteoric waters, which flowed downward along faults, or in aquifers, to locally replace the initial fluids.

Concerning sample SE10 and the 4 undated veins, because of the possibility of clumped isotope reordering, only their $\delta^{13}C$ values can be tentatively used to decipher the origin of the water that allowed their precipitation. The measured values are generally close to those observed for younger veins, consistent with marine or buffered water. Only SE10 vein has a $\delta^{13}C$ value significantly lower than that of the host rock (-4.5‰ versus -0.6‰). It indicates an organic origin of part of the carbon that could be soil derived or produced by microbially-mediated redox reactions (Hoefs, 2018).

Finally, the $\delta^{18}O$ of host rocks is too negative compared to those expected for marine sediments, with values below -2.4‰ (Figure 5C). For the Arguis-Pamplona marls, low values could be explained at least in part by the presence of a detrital carbonate fraction with negative signature. For the other formations, corresponding to platform carbonates, they necessarily indicate an alteration of the initial isotopic composition. It could result from burial recrystallization related to temperature increase, or from a partial reset during the ingress of large volumes of water in isotopic disequilibrium with the carbonates (e.g., Bradbury and Woodwell, 1987). A precise determination of the diagenetic evolution of the deposits involved in the SPFT would be necessary to determine the timing and conditions of such peculiar isotopic evolution, as well as to link it with the long-term evolution of calcite-precipitating water within the tectonic frame of the southern Pyrenees.

## Conclusions

The example of the South Pyrenean Frontal Thrust demonstrates the potential of $\Delta 47$/U-Pb thermo-chronometry to determine the conditions of fracture development and associated vein precipitation in tectonically complex areas such as fold and thrust belts. The ages obtained, which range between ~61 Ma and ~14 Ma, are sometimes clearly distinct from the estimates derived from the microstructural study of fractures, highlighting the relevance of absolute dating in fracture analysis. Most studied veins formed during the late exhumation of the area (age < 28 Ma), and the most recent ages obtained likely record the last tectonic pulses of the southern Pyrenees. This late formation makes it possible to validate the vein $T\Delta 47$

values, which were not modified by reordering during burial. Calculation of the oxygen isotopic compositions of the waters shows that the veins record either the incursion of meteoric water from the surface, or the presence of waters of more local origin that have interacted with the surrounding rocks. The modelling of the thermal evolution of the SPFT indicates that during maximum burial at around 28 Ma, temperatures could reach 120-140°C at the base of the series. For undated or older veins, clumped isotope reordering models suggest that such temperatures have been sufficient to significantly alter clumped isotopes values, excluding their use as a reliable thermal marker or paleohydrological tracer. Thus, in areas where temperatures higher than 100°C have been reached, the use of clumped on diagenetic calcite veins or cements should systematically be accompanied by the modelling of clumped isotope reordering. In this purpose defining the thermal history of the area under investigation is a mandatory pre-requisite, and determining the precipitation ages with the U-Pb method is a definite advantage.

**Acknowledgements**

This work benefited from a PhD grant of the French Ministry of Research (MESR) to NC. All analyses and field work performed in the course of this study were funded by a "CNRS excellence chair" grant to GH. The manuscript greatly benefited from the reviews of P. Granado and two anonymous reviewers.

**References**

Allen, P., Allen, J., 2013. Basin analysis: principles and application to petroleum play assessment (Third edition). Wiley-Blackwell, 632 p.

Anastasio, D.J., 1987. Thrusting, halotectonics, and sedimentation in the External Sierra, southern Pyrenees, Spain. PhD thesis, Johns Hopkins University, Baltimore, MD.

Arenas, C., Millán, H., Pardo, G., Pocoví, A., 2001. Ebro Basin continental sedimentation associated with late compressional Pyrenean tectonics (north-eastern Iberia): controls on basin margin fans and fluvial systems. Basin Res. 13, 65–89. https://doi.org/10. 1046/j.1365-2117.2001.00141.x.

Babault, J., Van Den Driessche, J., Bonnet, S., Castelltort, S., Crave, A., 2005. Origin of the highly elevated Pyrenean peneplain. Tectonics, 24, TC2010. doi:10.1029/ 2004TC001697.

Beaudoin, N., Lacombe, O., Roberts, N. M.W., Koehn, D., 2018. U-Pb dating of calcite veins reveals complex stress evolution and thrust sequence in the Bighorn Basin, Wyoming, USA. Geology, 46 (11), 1015-1018.

Beaudoin, N., Huyghe, D., Bellahsen, N., Lacombe, O., Emmanuel, L., Mouthereau, F., Ouanhnon, L., 2015. Fluid Systems and Fracture Development During Syn-Depositional Fold Growth: An Example from the Pico Del Aguila Anticline, Sierras Exteriores, Southern Pyrenees, Spain. J. Struct. Geol., 70, 23-38.

Beaumont, C., Muñoz, J.A., Hamilton, J., Fullsack, P., 2000. Factors Controlling the Alpine Evolution of the Central Pyrenees Inferred from a Comparison of Observations and Geodynamical Models. J. Geophys. Res.: Solid Earth, 105, 8121-8145.

Bergbauer, S., Pollard, D.D., 2004. A new conceptual fold-fracture model including prefolding joints, based on the Emigrant Gap anticline, Wyoming. GSA Bull., 116 (3-4), 294–307. doi: https://doi.org/10.1130/B25225.1

Bergman, S.C., Huntington, K.W., Crider, J.G., 2013. Tracing Paleofluid Sources Using Clumped Isotope Thermometry of Diagenetic Cements Along the Moab Fault, Utah. Am. J. Sci., 313, 490-515.

Bonifacie M., Calmels D., Eiler J.M., Horita, J., Chaduteau C., Vasconcelos, C., Agrinier, P., Katz A., Passey., B.H., Ferry J.M., Bourrand J.J., 2017. Experimental calibration of the dolomite clumped isotope thermometer from 25 to 350°C, and implications for a universal calibration for all (Ca, Mg, Fe)CO3 carbonates. Geochem. Cosmochem. Acta, 200, 255-279, doi: 10.1016/j.gca.2016.11.028

Bons, P.D., Elburg, M.A., Gomez-Rivas, E., 2012. A Review of the Formation of Tectonic Veins and Their Microstructures. J. Struct. Geol., 43, 33-62.

Bradbury, H.J., Woodwell, G.R., 1987. Ancient fluid flow within foreland terrains. In: Goff, J.C., Williams, B.P.J. (Eds.), Fluid Flow in Sedimentary Basins and Aquifers. Geological Society, London, Special Publications 34, 87–102.

Cantarelli, V., 2011. Tectonic-sedimentation Burial History and Exhumation of the Southern Sector of the Central-western Pyrenees. PhD Thesis, University of Camerino, Spain.

Carbayo, A., León, L., Puigdefàbregas, C., 1972, Mapa Geológico De España a Escala 1:50000. Hoja 117 (Ochagavía). IGME, Spain.

Carr, A., 2000. Suppression and Retardation of Vitrinite Reflectance, Part 1. Formation and Significance for Hydrocarbon Generation. J. Petr. Geol., 23, 313-343.

Choukroune, P., Roure, F., Pinet, B. & Team, E.P., 1990. Main Results of the Ecors Pyrenees Profile. Tectonophysics, 173, 411-423.

Coney, P. J., Muñoz, J.A., McClay, K.R., Evenchick, C.A., 1996. Syntectonic burial and post-tectonic exhumation of the southern Pyrenees foreland fold-thrust belt. J. Geol. Soc., London, 153, 9-16.

Crognier, N., Hoareau, G., Aubourg, C., Dubois, M., Lacroix, B., Branellec, M., Callot, J. P., Vennemann, T., 2018. Syn-orogenic fluid flow in the Jaca basin (south Pyrenean fold and thrust belt) from fracture and vein analyses. Bas. Res, 30, 187-216. doi:10.1111/bre.12249

Cruset, D., Cantarero, I., Benedicto, A., John, C.M., Vergés, J., Albert, R., Gerdes, A., Travé, A., 2020. From hydroplastic to brittle deformation: Controls on fluid flow in fold and thrust belts. Insights from the Lower Pedraforca thrust sheet (SE Pyrenees). Mar. Petr. Geol., 120, 104517, doi: https://doi.org/10.1016/j.marpetgeo.2020.104517.

De Rojas, B.J., Latorre, F., 1972. Mapa Geológico De España a Escala 1:50000. Hoja 175 (Sigüés). IGME, Spain.

Dennis, K.J., Affek, H.P., Passey, B.H., Schrag, D.P., Eiler, J.M., 2011. Defining an Absolute Reference Frame for 'Clumped' isotope Studies of $CO_2$. Geochem. Cosmochim. Acta, 75, 7117-7131.

Dromgoole, E.L., Walter, L.M., 1990. Iron and Manganese Incorporation into Calcite: Effects of Growth Kinetics, Temperature and Solution Chemistry. Chem. Geol., 81, 311-336.

Engelder, T., 1985. Loading paths to joint propagation during a tectonic cycle: an example from the Appalachian Plateau, J. Struct. Geol., 7, 459-476.

Filleaudeau, P.-Y., 2011. Croissance et dénudation des Pyrénées du Crétacé Supérieur au Paléogène : apports de l'analyse de bassin et thermochronométrie détritique. PhD thesis, Université Pierre et Marie Curie - Paris 6, Paris, France, 370 p.

Fitz-Diaz, E., Hudleston, P., Siebenaller, L., Kirschner, D., Camprubí, A., Tolson, G., Puig, T.P., 2011. Insights into fluid flow and water-rock interaction during deformation of carbonate sequences in the Mexican fold-thrust belt. J. Struct. Geol., 33, 1237-1253.

Garcia-Sansegundo, J., Montes, M.J., Garrido, E.A., Barnolas, A., A., B., 1992. Mapa Geológico De España a Escala 1:50000. Hoja 209 (Agüero). IGME, Spain.

Garven, G., 1985. The Role of Regional Fluid Flow in the Genesis of the Pine Point Deposit, Western Canada Sedimentary Basin. Econ. Geol., 80, 307-324.

Ghosh, P., Adkins, J., Affek, H., Balta, B., Guo, W., Schauble, E.A., Schrag, D., Eiler, J.M., 2006. 13 C–18 O Bonds in Carbonate Minerals: A New Kind of Paleothermometer. Geochem. Cosmochim. Acta, 70, 1439-1456.

Goldstein, R.H., Reynolds, T.J., 1994. Systematics of Fluid Inclusions in Diagenetic Minerals. Sepm Short Course 31, Society for Sedimentary Geology, 199 p.

Guo, W., Mosenfelder, J.L., Goddard, W.A., Eiler, J.M., 2009. Isotopic Fractionations Associated with Phosphoric Acid Digestion of Carbonate Minerals: Insights from First-Principles Theoretical Modeling and Clumped Isotope Measurements. Geochem. Cosmochim. Acta Acta, 73, 7203-7225.

Hoefs, J., 2018. Stable isotope geochemistry. Springer Textbooks in Earth Sciences, Geography and Environment, Springer, 437 p.

Hodson, K.R., Crider, J.G., Huntington, K.W., 2016. Temperature and Composition of Carbonate Cements Record Early Structural Control on Cementation in a Nascent Deformation Band Fault Zone: Moab Fault, Utah, USA. Tectonophysics, 690, 240-252, doi:10.1016/j.tecto.2016.04.032

Horstwood, MSA, Košler, J, Gehrels, G, Jackson, SE, Mclean, NM, Paton, C, Pearson, NJ, Sircombe, K, Sylvester, P, Vermeesch, P, Bowring, JF, Condon, DJ, Schoene, B., 2016. Community-Derived Standards for LA-ICP-MS U-(Th-)Pb Geochronology - Uncertainty Propagation, Age Interpretation and Data Reporting. Geostand. Geoanal. Res. 40(3), 311-332, doi :10.1111/j.1751-908X.2016.00379.x.

Huntington, K., Eiler, J., Affek, H., Guo, W., Bonifacie, M., Yeung, L., Thiagarajan, N., Passey, B., Tripati, A., Daëron, M., 2009. Methods and Limitations of 'Clumped' $CO_2$ Isotope (Δ47) Analysis by Gas-Source Isotope Ratio Mass Spectrometry. J. Mass Spectrom., 44, 1318-1329.

Huyghe, D., Mouthereau, F., Castelltort, S., Filleaudeau, P.Y., Emmanuel, L., 2009. Paleogene Propagation of the Southern Pyrenean Thrust Wedge Revealed by Finite Strain Analysis in Frontal Thrust Sheets: Implications for Mountain Building. Earth Planet. Sci. Lett., 288, 421-433.

Izquierdo-Llavall, E., Aldega, L., Cantarelli, V., Corrado, S., Gil-Peña, I., Invernizzi, C., Casas, A.M., 2013. On the Origin of Cleavage in the Central Pyrenees: Structural and Paleo-Thermal Study. Tectonophysics, 608, 303-318.

Kim, S.-T., O'Neil, J. R., 1997. Equilibrium and nonequilibrium oxygen isotope effects in synthetic carbonates Geochim. Cosmochim. Ac., 61, 3461–3475, 1997.

Labaume, P., Meresse, F., Jolivet, M., Teixell, A., Lahfid, A., 2016. Tectonothermal history of an exhumed thrust-sheet-top basin: An example from the south Pyrenean thrust belt. Tectonics, 35, doi:10.1002/ 2016TC004192.

Labaume, P., Teixell, 2018. 3D structure of subsurface thrusts in the eastern Jaca Basin, southern Pyrenees. Geol. Acta, 16-4, 477-498

Lacroix, B., Travé, A., Buatier, M., Labaume, P., Vennemann, T., Dubois, M., 2014. Syntectonic fluid-flow along thrust faults: Example of the South-Pyrenean fold-and-thrust belt. Mar. Petr. Geol., 49, 84-98.

Lacroix, B., Baumgartner, L., Bouvier, A.S., Kempton, P., Vennemann, T. 2018. Multi Fluid-Flow Record during Episodic Mode I Opening: A Microstructural and SIMS Study (Cotiella Thrust Fault, Pyrenees). Earth Planet. Sci. Lett. DOI 10.1016/j.epsl.2018.09.016

Lafargue E., Marquis, F., Pillot, D., 1998. Rock-Eval 6 applications in hydrocarbon exploration, production, and soil contamination studies: Rev. Inst. Fr. Pétr., 53, 4, 421–437.

Lawson M, Shenton BJ, Stolper DA, Eiler JM, Rasbury ET, Becker TP, Phillips-Lander C, Buono AS, Becker SP, Pottorf R, Gray GG, Yurewicz D, Gournay J, 2017. Deciphering the diagenetic history of the El Abra Formation of eastern Mexico using reordered clumped isotope temperatures and U-Pb dating. GSA Bull., 130(3–4), 617–629

Lloyd, M.K, Ryb, U., Eiler, J.M., 2018. Experimental calibration of clumped isotope reordering in dolomite. Geochim. Cosmochim. Acta, 242, 1–20

Longstaffe, F., 1987. Stable Isotope Studies of Diagenetic Processes. In: Short Course in Stable Isotope Geochemistry of Low Temperature Fluids (Ed. by T. K. Kyser), 13, 187-257. Mineralogical Association of Canada, Toronto.

Luetkemeyer, P.B., Kirschner, D.L., Huntington, K.W., Chester, J.S., Chester, F.M., Evans, J.P., 2016. Constraints on paleofluid sources using the clumped-isotope thermometry of carbonate veins from the SAFOD (San Andreas Fault Observatory at Depth) borehole. Tectonophysics, 690, 174–189.

MacDonald, J.M., Faithfull, J.W., Roberts, N.M.W., Davies, A.J.; Holdsworth, C.M., Newton, M., Williamson, S., Boyce, A., John, C.M. 2019. Clumped-isotope palaeothermometry and LA-ICP-MS. U–Pb dating of lava-pile hydrothermal calcite veins. Contrib. Mineral. Petrol., 174, 63. https://doi.org/10.1007/s00410-019-1599-x

Machel H.G., 2000. Application of Cathodoluminescence to Carbonate Diagenesis. In: Pagel M., Barbin V., Blanc P., Ohnenstetter D. (eds) Cathodoluminescence in Geosciences. Springer, Berlin, Heidelberg

Mangenot X., Gerdes A., Gasparrini M., Bonifacie M., Rouchon V., 2018. An emerging thermo-chronometer for carbonate-bearing rocks: Δ47/(U-Pb). Geology, 46(12), 1067-1070

Millán Garrido, H., Aurell, M., Meléndez, A. (1994) Synchronous Detachment Folds and Coeval Sedimentation in the Prepyrenean External Sierras (Spain): A Case Study for a Tectonic Origin of Sequences and Systems Tracts. Sedimentology, 41, 1001-1024.

Millán Garrido, H., Pueyo-Morer, E., Aurell-Cardona, M., Luzón-Aguado, A., Oliva-Urcia, B., Martínez-Peña, B., 2000. Actividad tectónica registrada en los depósitos terciarios del frente meridional del Pirineo central. Translated title: Tectonic activity recorded in the tertiary deposits of the southern front of the central Pyrenees. Rev. Soc. Geol. Esp., 13 (2), 279-300.

Mochales, T., Casas, A.M., Pueyo, E.L., Barnolas, A., 2012. Rotational velocity for oblique structures (Boltaña anticline, Southern Pyrenees): J. Struct. Geol., 35, 2-16.

Montes, M.J., Barnolas, A., 1992. Mapa Geológico De España a Escala 1:50000. Hoja 210 (Yebra De Basa). IGME, Spain.

Montes, M.J., Barnolas, A., 2002. Estratigrafia Del Eoceno - Oligoceno De La Cuenca De Jaca (Sinclinorio Del Guarga). PhD Tesis, Universidad de Barcelona, 365 p.

Muñoz J.A., 1992. Evolution of a continental collision belt: ECORS-Pyrenees crustal balanced cross-section. In: McClay K.R. (Eds.), Thrust Tectonics. Springer, Dordrecht, pp. 235–246.

Muñoz, J.A., 2002. Alpine tectonics I: the Alpine system north of the Betic Cordillera. Tectonic setting; The Pyrenees. In: W. Gibbons, T. Moreno (Eds.), Geology of Spain, Geol. Soc (London), pp. 370-385.

Muñoz, J.-A., Beamud, E., Fernández, O., Arbués, P., Dinarès-Turell, J., Poblet, J. 2013. The Ainsa Fold and thrust oblique zone of the central Pyrenees: Kinematics of a curved contractional system from paleomagnetic and structural data, Tectonics, 32, 1142- 1175, doi:10.1002/tect.20070.

Muñoz, J.A., Mencos, J., Roca, E., Carrera, N., Gratacós, O., Ferrer, O., Fernández, O., 2018. The structure of the South-Central-Pyrenean fold and thrust belt as constrained by subsurface data. Geol. Acta, 16 (4), 439-460.

Ogg, J.G., Ogg, G.M., Gradstein, F.M., 2016. A Concise Geological Time Scale. Elsevier, 229 p.

Oliva-Urcia, B., Pueyo, E. L., 2007. Rotational basement kinematics deduced from remagnetized cover rocks (Internal Sierras, southwestern Pyrenees), Tectonics, 26, TC4014, doi:10.1029/2006TC001955.

Oliva-Urcia, B., Beamud, E., Garcés, M., Arenas, C., Soto, R., Pueyo, E.L., Pardo, G., 2016. New magnetostratigraphic dating of the Palaeogene syntectonic sediments of the west-central Pyrenees: tectonostratigraphic implications. In: Pueyo, E.L., Cifelli, F., Sussman, A.J., Oliva-Urcia, B. (Eds.), Palaeomagnetism in Fold and Thrust Belts: New Perspectives. Geological Society, London, Special Publications, vol. 425. pp. 107–128. https://doi.org/10.1144/SP425.5.

Oliva-Urcia, B., E. Beamud, C. Arenas, E.L. Pueyo, M. Garcés, R. Soto, L. Valero, F.J. Pérez-Rivarés, 2019. Dating the northern deposits of the Ebro foreland basin; implications for the kinematics of the SW Pyrenean front, Tectonophysics, Volume 765, 2019, 11-34, https://doi.org/10.1016/j.tecto.2019.05.007.

Price L.C., Barker, C.E., 1985. Suppression of vitrinite reflectance in amorphous rich kerogen - A major unrecognized problem: J. Petr. Geol., 8, 59-84

Pueyo, E., Millán, H., Pocovi, A., 2002. Rotation Velocity of a Thrust: A Paleomagnetic Study in the External Sierras (Southern Pyrenees). Sed. Geol., 146, 191-208.

Roberts, N.M., Walker, R.J., 2016. U-Pb Geochronology of Calcite-Mineralized Faults: Absolute Timing of Rift-Related Fault Events on the Northeast Atlantic Margin. Geology, G37868. 37861.

Roberts, N.M.W., Rasbury, E.T., Parrish, R.R., Smith, C.J., Horstwood, M.S.A., Condon, D.J., 2017. WC-1: A calcite reference material for LA-ICP-MS U-Pb geochronology, Geochem., Geophys., Geosyst., 18, 2807-2814, doi: 10.1002/2016GC006784.

Roure, F., Swennen, R., Schneider, F., Faure, J., Ferket, H., Guilhaumou, N., Osadetz, K., Robion, P., Vandeginste, V., 2005. Incidence and Importance of Tectonics and Natural Fluid Migration on Reservoir Evolution in Foreland Fold-and-Thrust Belts. Oil & gas sci. technol., 60, 67-106.

Samso, J.M., Sanz, J., Garcia, J., Serra, J., Tosquella, J., Garrido, E.A., Barnolas, A., 1991. Mapa Geológico De España a Escala 1:50000. Hoja 248 (Apiés). IGME, Spain.

Soler-Sampere, M., Puigdefàbregas, C., 1970. Líneas Generales De La Geología Del Alto Aragón Occidental. Pirineos, 96, 5-20

Stolper, D.A., Eiler, J.M., 2015. The Kinetics of Solid-State Isotope-Exchange Reactions for Clumped Isotopes: A Study of Inorganic Calcites and Apatites from Natural and Experimental Samples. Am. J. Sci., 315, 363-411.

Tavani, S., Storti, F., Lacombe, O., Corradetti, A., Munoz, J. Mazzoli, S., 2015. A review of deformation pattern templates in foreland basin systems and fold-and-thrust belts: implications for the state of stress in the frontal regions of thrust wedges. Earth Sci. Rev., 141, 82–104.

Teixell, A., Montes, M.J., Arenas, C., Garrido, E.A., 1992. Mapa Geológico De España a Escala 1:50000. Hoja 208 (Uncastillo). IGME, Spain.

Teixell, A., 1996. The Ansó transect of the southern Pyrenees: basement and cover thrust geometries. Journal of the Geological Society, 153(2), 301-310. https://doi.org/10.1144/gsjgs.153.2.0301

Teixell, A, Labaume, P, Ayarza, P, Espurt, N, de Saint Blanquat, M, Lagabrielle, Y., 2018. Crustal structure and evolution of the Pyrenean-Cantabrian belt: A review and new interpretations from recent concepts and data. Tectonophysics, 724-725, 146-170. https://doi.org/10.1016/j.tecto.2018.01.009

Travé A., Labaume P., Vergés J., 2007. Fluid Systems in Foreland Fold-and-Thrust Belts: An Overview from the Southern Pyrenees. In: Lacombe O., Roure F., Lavé J., Vergés J. (Eds), Thrust Belts and Foreland Basins. Frontiers in Earth Sciences. Springer, Berlin, Heidelberg, pp. 93-115. https://doi.org/10.1007/978-3-540-69426-7_5

Travé, A., Labaume, P., Calvet, F., Soler, A., 1997. Sediment Dewatering and Pore Fluid Migration Along Thrust Faults in a Foreland Basin Inferred from Isotopic and Elemental Geochemical Analyses (Eocene Southern Pyrenees, Spain). Tectonophysics, 282, 375-398.

Turner, J., 1988. Tectonic and Stratigraphic Evolution of the West Jaca Thrust-Top Basin, Southwest Pyrenees, PhD thesis, University of Bristol.

Twiss, R.J., Moores, E.M., 2006. Structural Geology, 2nd edition, Freeman & Co, 532 p.

Vilasi, N., Malandain, J., Barrier, L., Callot, J.P., Guilhaumou, N., Lacombe, O., Muska, K., Roure, F., Swennen, R. (2009). From outcrop and petrographic studies to basin-scale fluid flow modelling: the use of the Albanian natural laboratory for carbonate reservoir characterization, Tectonophysics, 474, 367-392.

Zachos, J., Pagani, M., Sloan, L., Thomas, E, Billups, K., 2001. Trends, Rhythms, and Aberrations in Global Climate 65 Ma to Present. Science, 292, 686-693.

## TABLES

**Table S1**: Results of isotopic, microthermometric and U-Pb dating measurements for the studied veins and their host-rocks.

**Table S2**: calcite U-Pb analyses for standards (WC1, Duff Brown) and successful samples (SE3, SE4, SE10, A21, A22, A56)

**Table S3**: Results of Rock-Eval Tmax analyses

# Figure captions

**Figure 1**. A: Simplified geological map of the Pyrenees (modified from Filleaudeau, 2011). The black line locates the cross-section in B, and the red frame the studied area in C. B: Balanced cross section of the Jaca Basin including the Sierras Exteriores to the south (modified from Labaume et al., 2016 and Labaume and Teixell, 2018). C: Geological map of the Sierras Exteriores based on Garcia-Sansegundo et al. (1992), Samso et al. (1991) and Teixell et al. (1992), with location of the studied sites and samples. D, E: closer views of the two main areas investigated. Symbols refer to the type of analysis made on the samples (see key). Virtual sedimentary logs: 1: San Felices; 1-2: Riglos and top San Felices; 3: Nueno; 3-4: Pico Del Aguila and top Nueno.

**Figure 2**: Results of fracture analysis in 7 of the 10 studied sites. Results are presented on 3 diagrams (Schmidt' lower-hemisphere, equal-area stereonets) displaying raw data in current bedding attitude (left), corrected for fold axial plunge related to the Guarga thrust activation (middle) and corrected for local bedding dip (right). See text for details. For site A22, where the sampled vein corresponds to a right-lateral fault, the stereogram represents the results of fault-slip inversion calculations, and is directly taken from Beaudoin et al. (2015). Computed stress axes are reported as stars with three branches ($\sigma 1$), four branches ($\sigma 2$) and five branches ($\sigma 3$). Convergent black arrows indicate the direction of compression.

**Figure 3**: A. Close field view of vein SE3 (arrows). B. Field photograph of vein SE10 (arrows, highlighted in black). The fracture network as well as two faults (green arrows) are visible. Red dots refer to the orientation of bedding. C. Field view of site SE4. Arrows point to fractures belonging the dominant fracture set. Red dots refer to the orientation of bedding.

D. Field view of site SE12, characterized by a complex fracture network. Red dots refer to the orientation of bedding. E. Mosaics of optical (PPL) and CL photomicrographs across vein SE1. Green arrow points to a stretched crystal typical of syn-opening growth. White arrow points to void-filling calcite with brighter orange CL (see text). Scale bar = 1 mm. F. Optical (PPL) and CL photomicrographs of vein A56, with a blocky texture. Scale bar = 1 mm.

**Figure 4:** A to E: Mosaics of optical and CL photomicrographs across calcite veins. Scale bars = 1 mm. A. Vein SE4. Stylolites affecting blocky calcites are visible (white arrows). B: Vein A22. In XPL, an increase of grain size is observed towards the center of the vein (left to right). The arrow points to a limit interpreted as reflecting a stage of vein opening. In CL, the color slightly differs on each side of this discontinuity. White line defines the vein border. C. Vein SE2. Numerous shear-related calcite sheets (parallel to the vein wall, here vertical) can be identified. D. Vein SE10. Several generations of blocky calcite can be identified both in PPL and CL. Minor brecciation is also visible to the right of the images. E. Vein SE3. Concentric zoning can be seen on the blocky calcite grains in CL. It follows the trails of primary fluid inclusions visible in XPL (arrows).

**Figure 5** A. Histogram of homogenization temperatures measured in primary fluids inclusions. Note that for SE10, most fluid inclusions are all liquid. B: Comparison of temperatures obtained with clumped isotopes (using the calibration of Bonifacie et al. (2017) (stars) and with fluid inclusions (bars). Colors of the stars correspond to the age of host-rocks (see legend). C: $\delta^{18}O$ versus $\delta^{13}C$ plot of veins and related host-rocks. The numbers refer to sample labels (ex: 56 for A56, 3 for S3, etc). D: Isotopic composition of water calculated from oxygen isotope data of veins and associated clumped isotope temperatures, using the equation of Kim and O'Neil (1997) (all replicates are shown).

**Figure 6**: Tera-Wasserburg diagrams for the 6 veins successfully dated by the U-Pb method. Red ellipses were not considered in the age calculation. All ellipses correspond to 2 sigma uncertainties.

**Figure 7**: Results of 1D thermal modelling for the four virtual time-correlated sedimentary logs compiled from previously published logs (see references in the data repository, and location of samples and sections in Figure 1). Stars refer to the age of rocks hosting the veins analyzed for clumped isotopes. For each log, the red dotted frame (upper part of the Campodarbe Fm) corresponds to the thickness of currently eroded sediments that has been added to the model to fit the maturity data (see text for details). Chronostratigraphic correlations from Samso et al. (1991), Garcia-Sansegundo et al. (1992), Teixell et al. (1992), Montes and Barnolas (2002) and Oliva-Urcia et al. (2016). Tectonic stages from Labaume et al. (2016). Magnetostratigraphic scale from Ogg et al. (2016).

**Figure 8**: Time-temperature paths for the rocks hosting the 10 veins analyzed for clumped isotopes, as deduced from 1D thermal modelling. The U-Pb ages of dated veins, as well as the range of possible vein precipitation ages calculated from $T\Delta 47$ and assuming thermal equilibrium with the host rocks are indicated. Two exhumation paths are represented (orange and red curves; see text for detail).

**Figure 9**: A. Modelling of the reordering behavior of calcite $T\Delta 47$ (THRM) using the exchange-diffusion model of Stolper and Eiler (2015) and 1D thermal models of the study area. Shaded areas correspond to 2s uncertainties. The measured range of $T\Delta 47$ is indicated between the grey dashed lines. A: Evolution of $T\Delta 47$ for SE10 vein, using 3 distinct starting

precipitation temperatures at 60 Ma (20, 43 and 80°C). In the three scenarios, the modelled present-day T$\Delta$47 is similar to the measured values within uncertainties. B, C: Evolution of T$\Delta$47 for SE2 vein for several precipitation ages (ranging from 36 to 20 Ma), and precipitation temperatures similar to the enclosing rock. The results for burial and exhumation paths have been represented on two distinct graphs for clarity (B and C, respectively). See text for explanations.

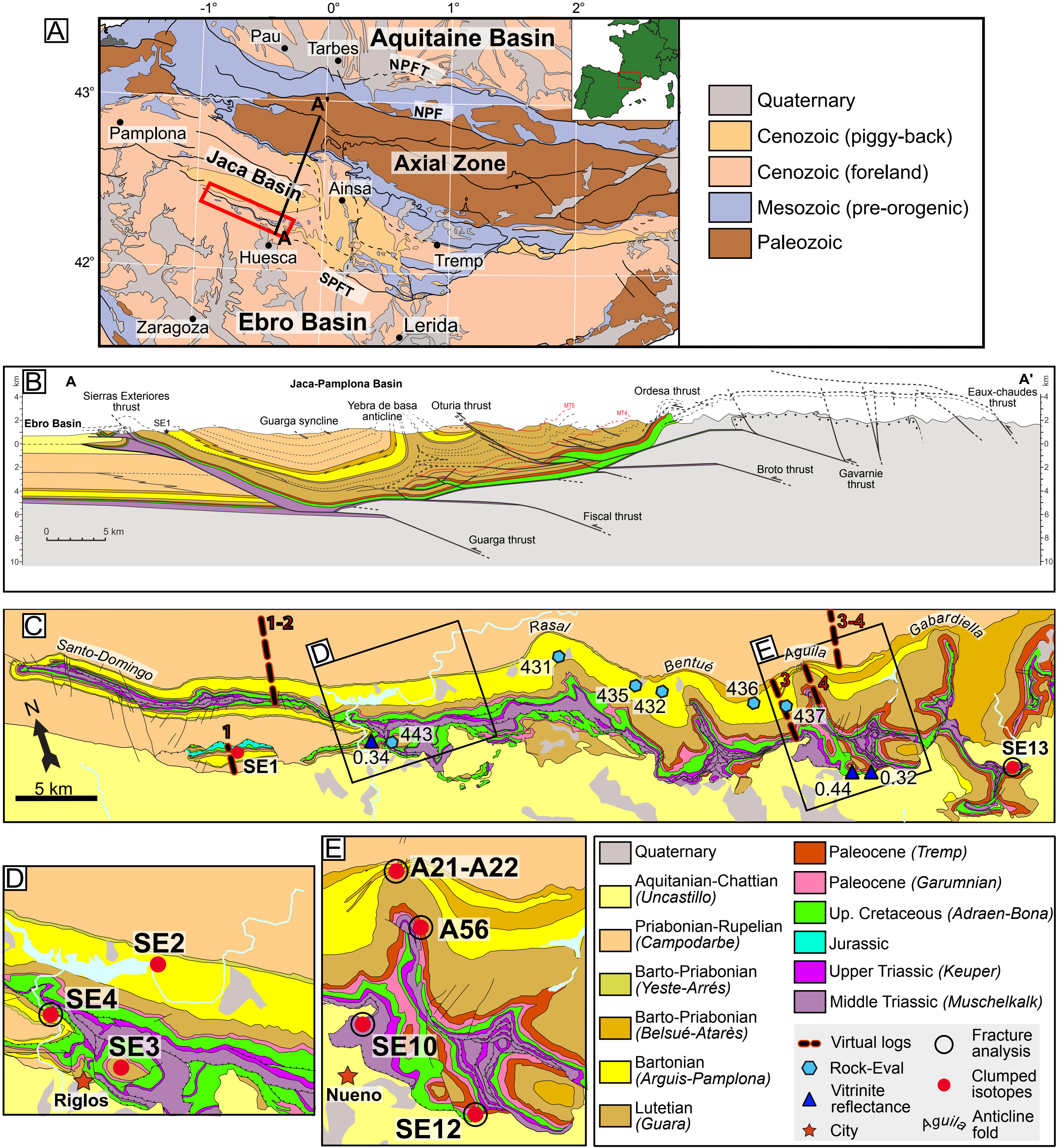
A
-1°
0°
1°
2°
43°
42°
Pau
Tarbes
Aquitaine Basin
NPFT
NPF
A'
Pamplona
Axial Zone
Jaca Basin
Ainsa
A
Huesca
Tremp
SPFT
Zaragoza
Ebro Basin
Lerida
Quaternary
Cenozoic (piggy-back)
Cenozoic (foreland)
Mesozoic (pre-orogenic)
Paleozoic
B
A
A'
Jaca-Pamplona Basin
Sierras Exteriores thrust
SE1
Ebro Basin
Guarga syncline
Yebra de basa anticline
Oturia thrust
MT5
MT4
Ordesa thrust
Eaux-chaudes thrust
Broto thrust
Gavarnie thrust
Fiscal thrust
Guarga thrust
km
0
5 km
C
Santo-Domingo
1-2
D
Rasal
431
435
432
Bentué
436
E
Aguila
3-4
3
4
437
Gabardiella
1
SE1
443
0.34
0.44
0.32
SE13
N
5 km
D
SE2
SE4
SE3
Riglos
E
A21-A22
A56
SE10
Nueno
SE12
Quaternary
Aquitanian-Chattian (Uncastillo)
Priabonian-Rupelian (Campodarbe)
Barto-Priabonian (Yeste-Arrés)
Barto-Priabonian (Belsué-Atarès)
Bartonian (Arguis-Pamplona)
Lutetian (Guara)
Paleocene (Tremp)
Paleocene (Garumnian)
Up. Cretaceous (Adraen-Bona)
Jurassic
Upper Triassic (Keuper)
Middle Triassic (Muschelkalk)
Virtual logs
Rock-Eval
Vitrinite reflectance
City
Fracture analysis
Clumped isotopes
Aguila
Anticline fold

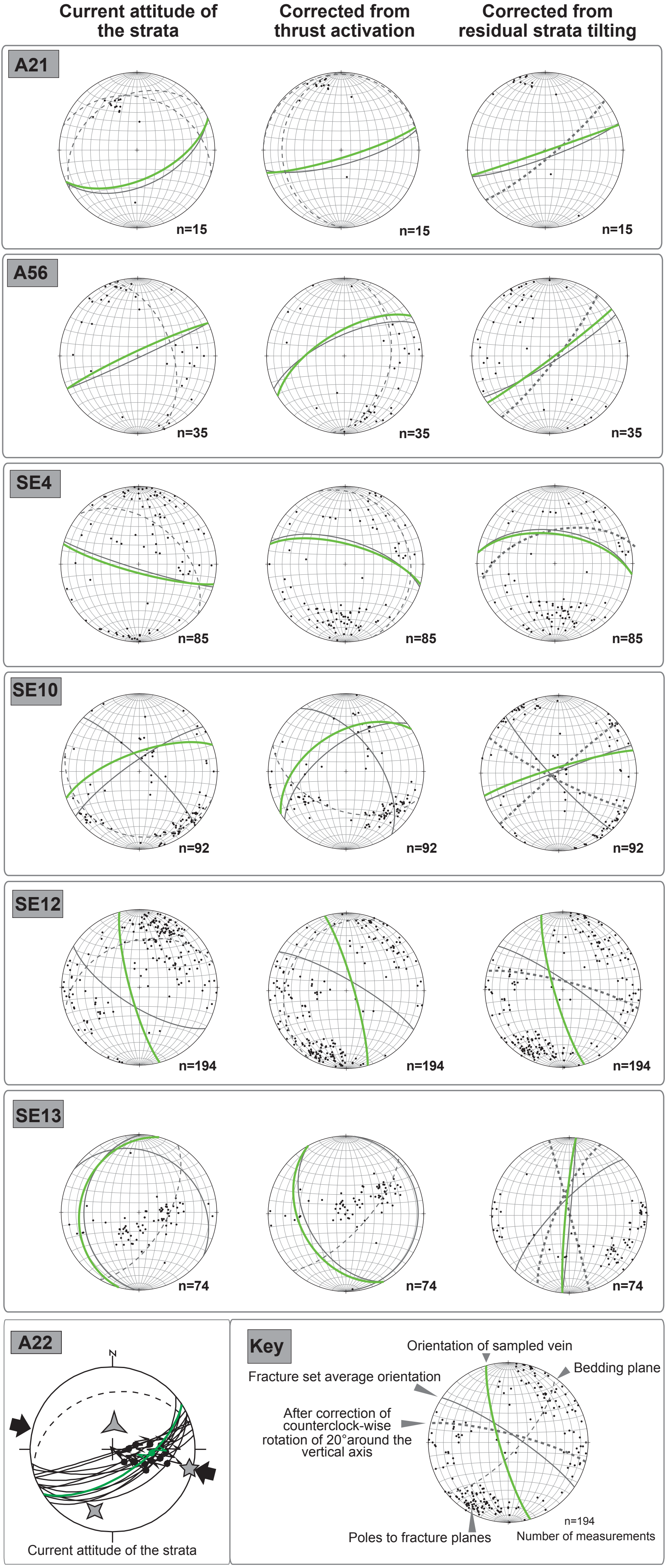
Current attitude of the strata
Corrected from thrust activation
Corrected from residual strata tilting
A21
n=15
A56
n=35
SE4
n=85
SE10
n=92
SE12
n=194
SE13
n=74
A22
N
Current attitude of the strata
Key
Orientation of sampled vein
Bedding plane
Fracture set average orientation
After correction of counterclock-wise rotation of 20°around the vertical axis
Poles to fracture planes
n=194
Number of measurements

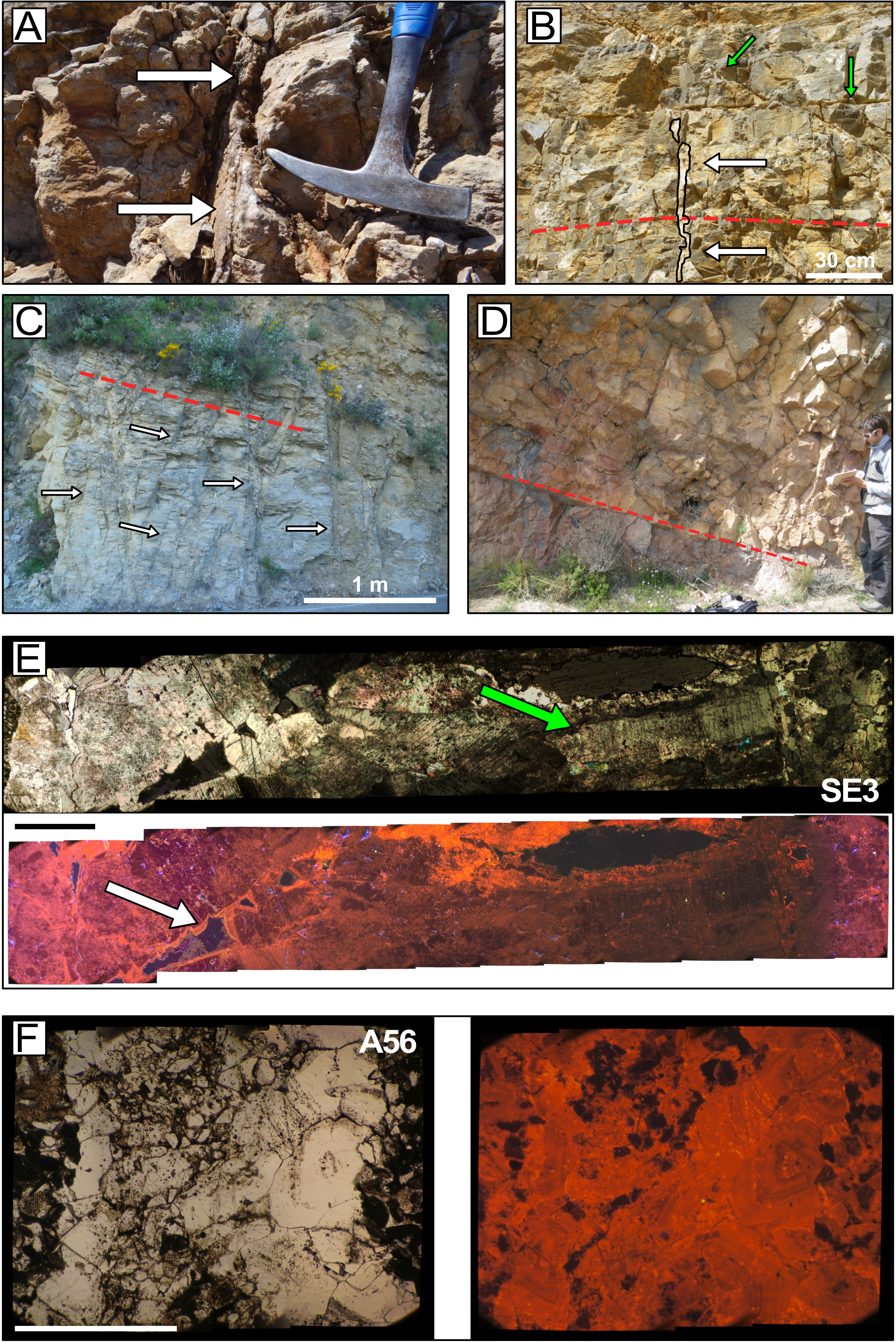
A
B
30 cm
C
1 m
D
E
SE3
F
A56

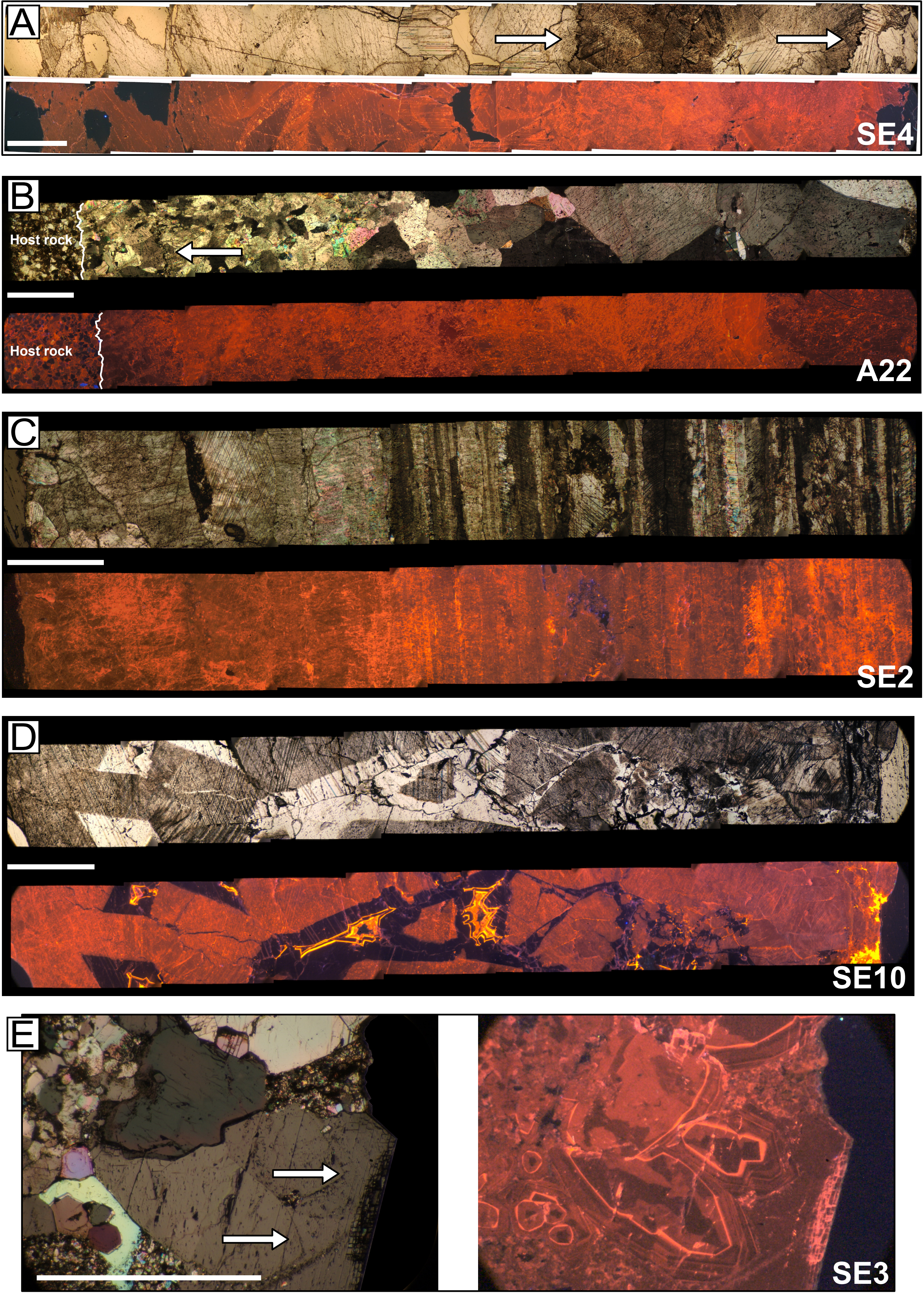
A
SE4
B
Host rock
Host rock
A22
C
SE2
D
SE10
E
SE3

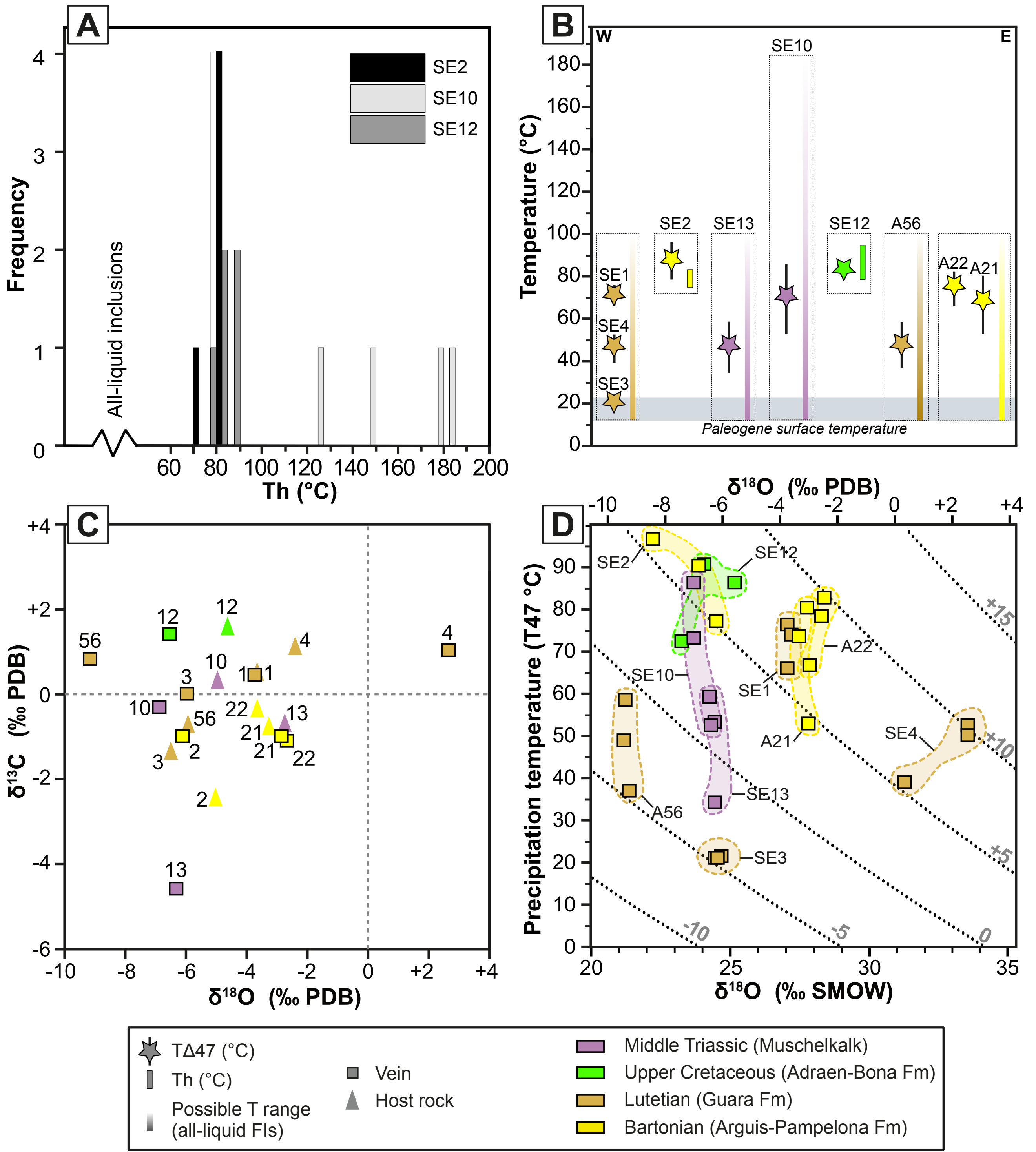
A
B
C
D
Frequency
Th (°C)
All-liquid inclusions
SE2
SE10
SE12
Temperature (°C)
W
E
SE1
SE4
SE3
SE13
A56
A22
A21
Paleogene surface temperature
δ18O (‰ PDB)
δ13C (‰ PDB)
Precipitation temperature (T47 °C)
δ18O (‰ SMOW)
TΔ47 (°C)
Th (°C)
Possible T range (all-liquid FIs)
Vein
Host rock
Middle Triassic (Muschelkalk)
Upper Cretaceous (Adraen-Bona Fm)
Lutetian (Guara Fm)
Bartonian (Arguis-Pampelona Fm)

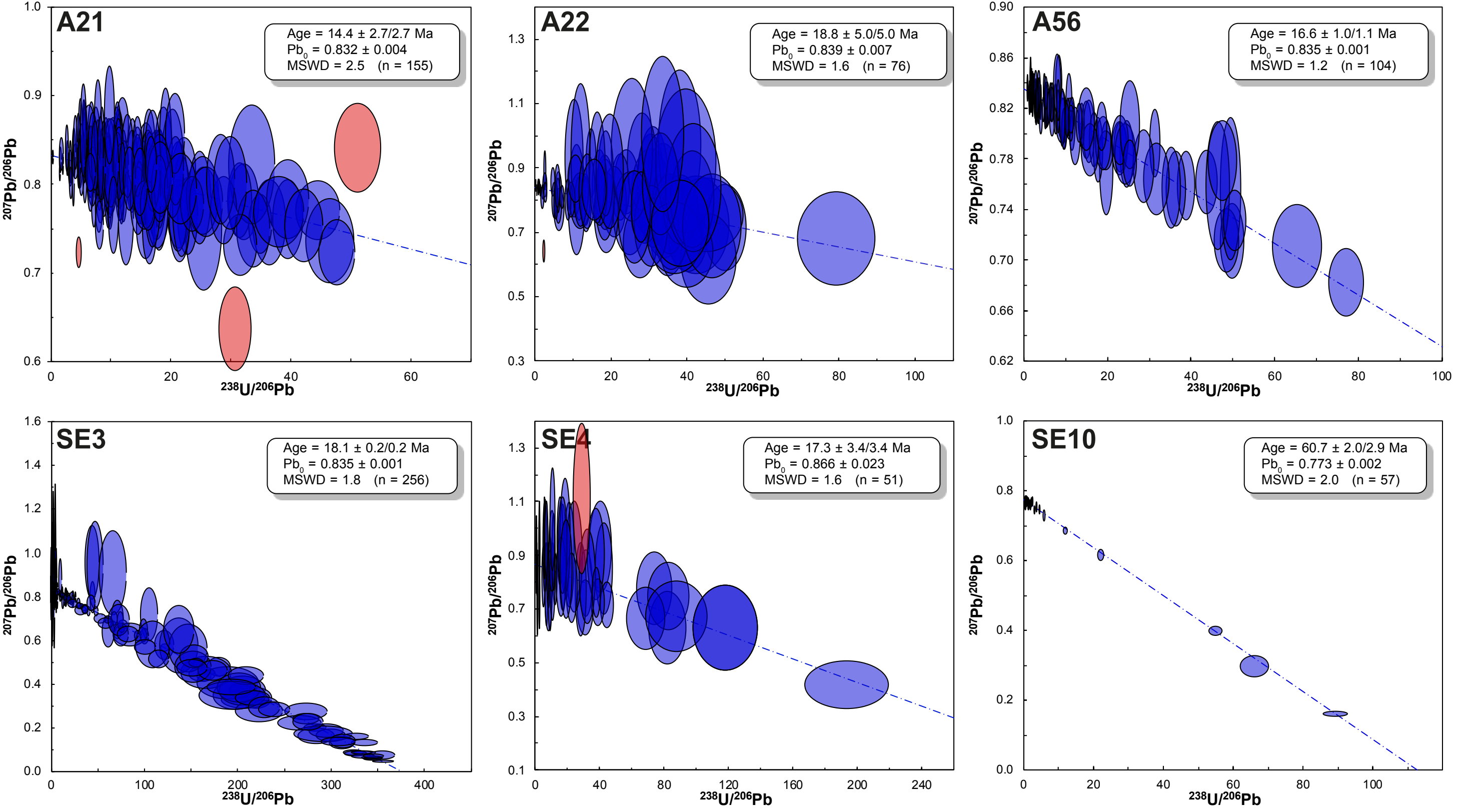

A21
Age = 14.4 ± 2.7/2.7 Ma
Pb0 = 0.832 ± 0.004
MSWD = 2.5 (n = 155)
A22
Age = 18.8 ± 5.0/5.0 Ma
Pb0 = 0.839 ± 0.007
MSWD = 1.6 (n = 76)
A56
Age = 16.6 ± 1.0/1.1 Ma
Pb0 = 0.835 ± 0.001
MSWD = 1.2 (n = 104)
SE3
Age = 18.1 ± 0.2/0.2 Ma
Pb0 = 0.835 ± 0.001
MSWD = 1.8 (n = 256)
SE4
Age = 17.3 ± 3.4/3.4 Ma
Pb0 = 0.866 ± 0.023
MSWD = 1.6 (n = 51)
SE10
Age = 60.7 ± 2.0/2.9 Ma
Pb0 = 0.773 ± 0.002
MSWD = 2.0 (n = 57)
207Pb/206Pb
238U/206Pb

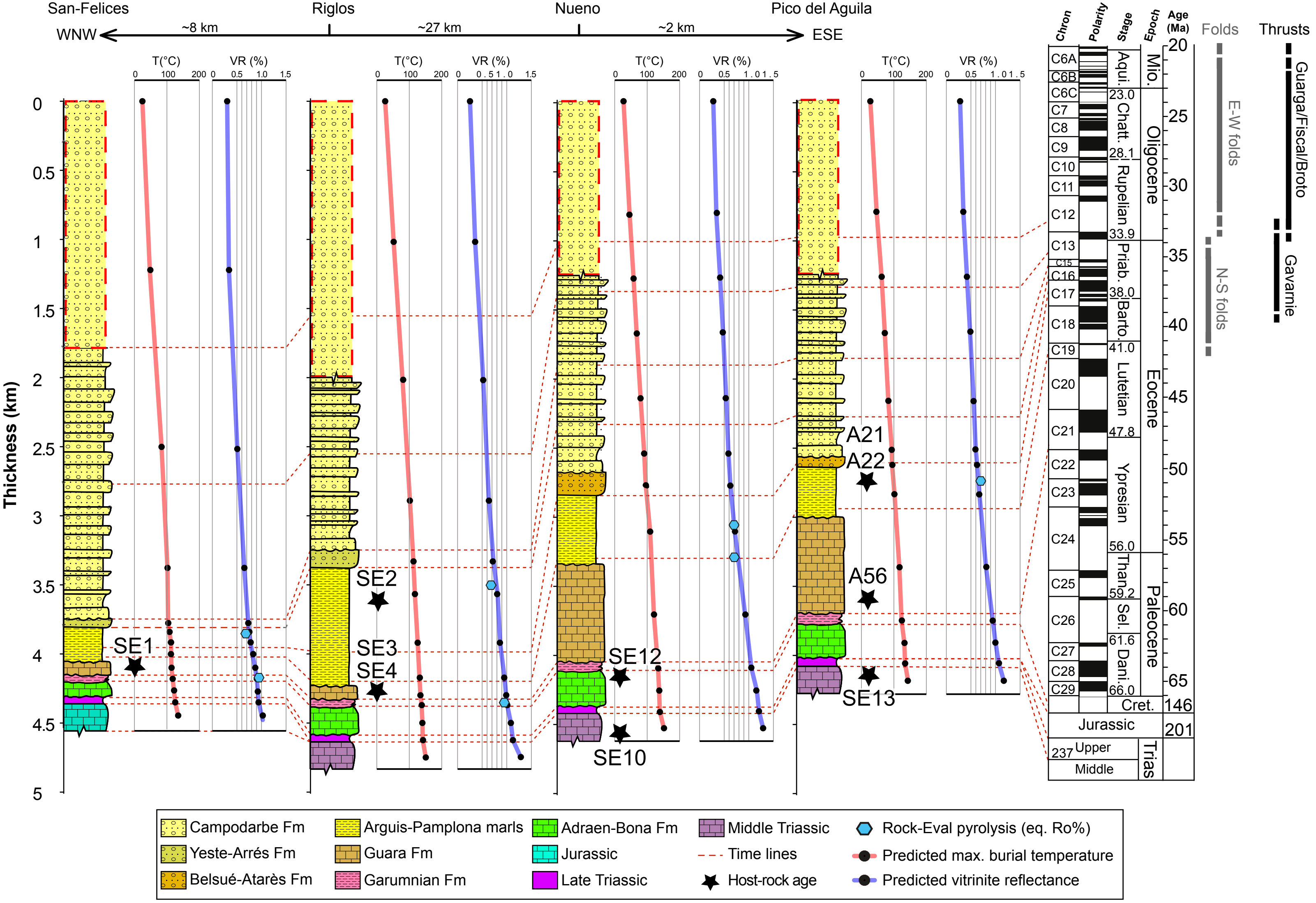

San-Felices
Riglos
Nueno
Pico del Aguila
WNW
ESE
~8 km
~27 km
~2 km
Thickness (km)
T(°C)
VR (%)
SE1
SE2
SE3
SE4
SE12
SE10
SE13
A21
A22
A56
Chron
Polarity
Stage
Epoch
Age (Ma)
Folds
Thrusts
E-W folds
N-S folds
Guarga/Fiscal/Broto
Gavarnie
Mio.
Oligocene
Eocene
Paleocene
Aqui.
Chatt.
Rupelian
Priab.
Barto.
Lutetian
Ypresian
Than.
Sel.
Dani.
Cret.
Jurassic
Upper
Middle
Trias
Campodarbe Fm
Yeste-Arrés Fm
Belsué-Atarès Fm
Arguis-Pamplona marls
Guara Fm
Garumnian Fm
Adraen-Bona Fm
Jurassic
Late Triassic
Middle Triassic
Time lines
Host-rock age
Rock-Eval pyrolysis (eq. Ro%)
Predicted max. burial temperature
Predicted vitrinite reflectance

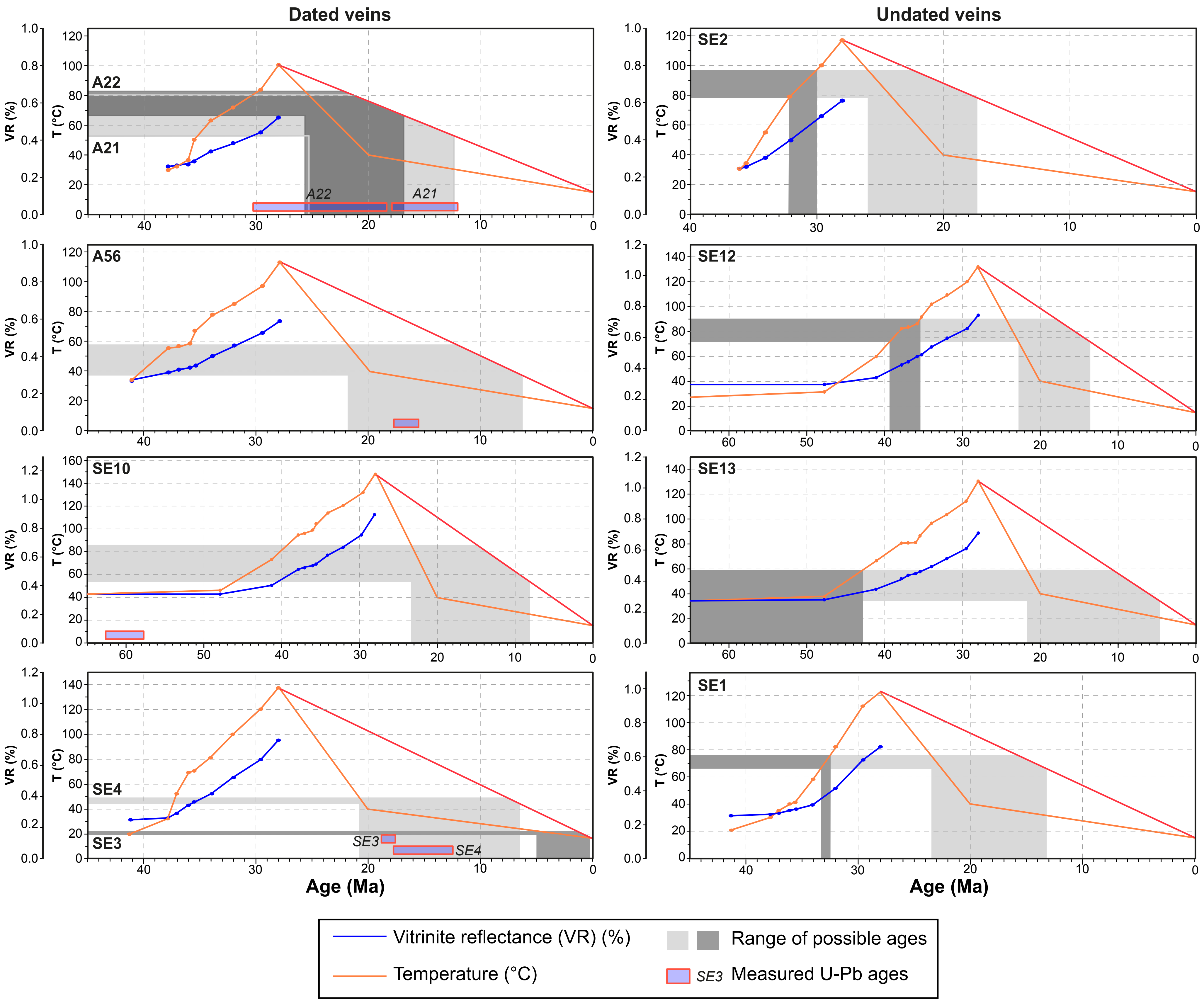

Dated veins
Undated veins
A22
A21
A56
SE10
SE4
SE3
SE2
SE12
SE13
SE1
VR (%)
T (°C)
Age (Ma)
Vitrinite reflectance (VR) (%)
Temperature (°C)
Range of possible ages
SE3 Measured U-Pb ages

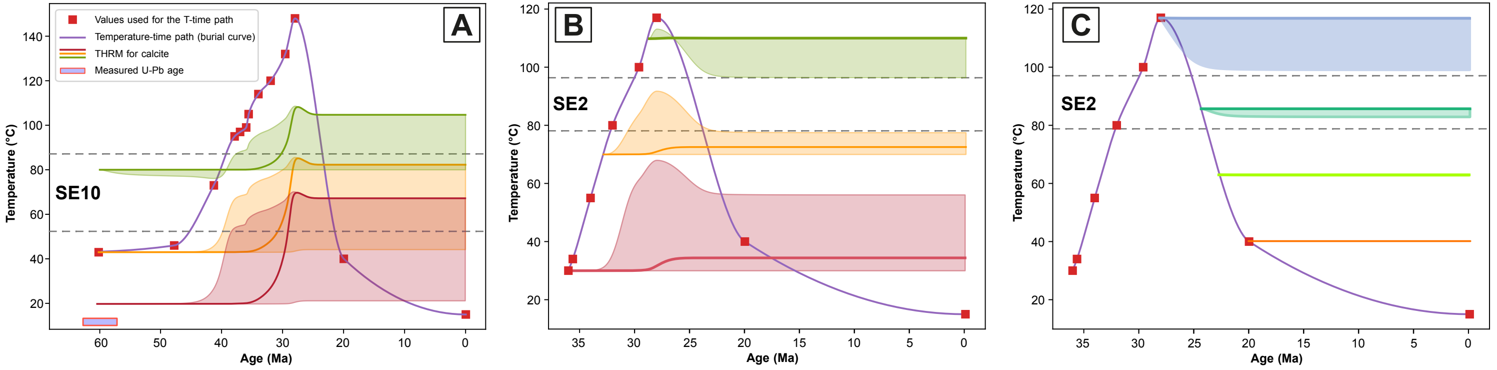

A
Values used for the T-time path
Temperature-time path (burial curve)
THRM for calcite
Measured U-Pb age
SE10
Temperature (°C)
Age (Ma)
B
SE2
Temperature (°C)
Age (Ma)
C
SE2
Temperature (°C)
Age (Ma)